University of Illinois at Urbana-Champaign

ACRC

Air Conditioning and Refrigeration Center A National Science Foundation/University Cooperative Research Center

Design Tool for Display Case Heat Exchanger Frosting and Defrosting

P. Verma, C. W. Bullard and P. S. Hrnjak

ACRC TR-201 October 2002

For additional information:

Air Conditioning and Refrigeration Center
University of Illinois
Mechanical & Industrial Engineering Dept.
1206 West Green Street
Urbana, IL 61801

(217) 333-3115

Prepared as part of ACRC Project #119
Evaporator Frosting and Optimal Defrost Frequency
P. S. Hrnjak and C. W. Bullard, Principal Investigators

The Air Conditioning and Refrigeration Center was founded in 1988 with a grant from the estate of Richard W. Kritzer, the founder of Peerless of America Inc. A State of Illinois Technology Challenge Grant helped build the laboratory facilities. The ACRC receives continuing support from the Richard W. Kritzer Endowment and the National Science Foundation. The following organizations have also become sponsors of the Center.

Alcan Aluminum Corporation
Amana Refrigeration, Inc.
Arçelik A. S.
Brazeway, Inc.
Carrier Corporation
Copeland Corporation
Dacor
Daikin Industries, Ltd.
Delphi Harrison Thermal Systems
General Motors Corporation
Hill PHOENIX
Honeywell, Inc.
Hydro Aluminum Adrian, Inc.
Ingersoll-Rand Company
Kelon Electrical Holdings Co., Ltd.
Lennox International, Inc.
LG Electronics, Inc.
Modine Manufacturing Co.
Parker Hannifin Corporation
Peerless of America, Inc.
Samsung Electronics Co., Ltd.
Tecumseh Products Company
The Trane Company
Valeo, Inc.
Visteon Automotive Systems
Wolverine Tube, Inc.
York International, Inc.

For additional information:

Air Conditioning & Refrigeration Center
Mechanical & Industrial Engineering Dept.
University of Illinois
1206 West Green Street
Urbana, IL 61801

217 333 3115

Abstract

A simulation model for predicting the performance of a display case under frosting conditions has been developed. An experimentally validated heat exchanger simulation model for a secondary refrigerant was extended to simulate operation in open display cases, modeling the varying frost properties and operating conditions and their effect on heat exchanger performance. A separate model based on a few simplifying assumptions has been developed to simulate the defrosting, predict the time required to melt the frost mass (existing at the end of frosting cycle) and compressor and fan power requirements for an entire day operation of a display case.

Two design strategies for reducing defrost frequency and overall energy consumption of open supermarket display cases were evaluated relative to the baseline (variable air flow as a consequence of fan characteristics) operation: constant air flow operation; and fin staging.

A preliminary analysis of a flat-tube-plain-fin heat exchanger with discontinuous fins was also conducted A simple comparison of heat transfer performance at dry surface conditions shows that all the designs considered are better than an existing display case round-tube-plain-fin heat exchanger.

Table of Contents

List of Figures

List of Tables

Page

Nomenclature

A	surface area, m^2
af	ambient air entrainment fraction
A_{free}	air free flow area, m^2
cfm	air flow rate , *cfm*
COP	coefficient of performance
c_p	specific heat of moist air, *kJ/kg.K*
Dc	tube collar diameter, *m*
D_h	hydraulic diameter, *m*
d_i	tube internal diameter, *m*
dP	pressure drop, *Pa*
dT	temperature drop, ^oC
E	thermal energy, *kJ*
f	Darcy's friction factor
fn	fin
fpm	fins per m, m^{-1}
f_{th}	fin thickness, *m*
Fs, F_P	fin pitch, *m*
g	acceleration due to gravity, m/s^2
G	mass flux, $kg/m^2.s$
h	enthalpy of dry air, *kJ/kg*
H	height of the heat exchanger, *m*
h_a	convective airside heat transfer coefficient, $kW/m^2.K$
h_{ref}	refrigerant side heat transfer coefficient, $kW/m^2.K$
h_{sg}	latent heat of ablimation or sublimation of water @ T_{so}, *kJ/kg*
j	Colburn's dimensionless heat transfer coefficient
K_a	thermal conductivity of air, *kW/m.K*
k_{fr}	thermal conductivity of frost, *kW/m.K*
L	fin length (along air flow) for a finite volume, *m*
Le	Lewis number, *a/D*
Len	length
LMTD	log mean temperature difference, ^oC
M	molecular weight
m_{frost}	mass of frost deposited, *kg*
$\dot{m}_{fr}$	frost deposition rate, *kg/s*
$\dot{m}_{air}$	air mass flow rate, *kg/s*
$\dot{m}_{melt}$	frost melting rate, *kg/s*
$\dot{m}_{ref}$	refrigerant mass flow rate, *kg/s*
N_{fin}	number of fins for a finite volume
N_{tube}	number of tubes for a finite volume
Nu	Nusselt number
NTU	number of transfer units
Q	load on evaporator, *kW*

$\dot{Q}$	energy, *kW*
Pr	Prandtl number
P	pressure, *Pa*
P_l, S_l	longitudinal tube spacing (along air flow direction), *m*
P_t, S_t	transverse tube spacing (transverse to air flow direction), *m*
r	distance from the center of the tube, *m*
raf	refrigerant void fraction
Re	Reynolds number
RH	relative humidity
S_l	see P_l
S_t	see P_t
T	temperature, ^oC
tb	tube
v	specific volume, m^3/kg
$\dot{V}$	volumetric flow rate, m^3/s
V_{max}	velocity of air based on free flow area, *m/s*
Vol	package (heat exchanger core) volume, m^3
V	velocity, *m/s*
w	air absolute humidity, kg_{water}/kg_{air}
W	width of heat exchanger, *m*
$\dot{W}$	power, *kW*
x	vapor mass fraction of refrigerant
z	number of fins in direction of air flow (z = 1 for a continuous fin)
z_r	number of tubes in individual fin in direction of air flow
f_{sl}	friction factor for the slot between two fins without tubes

Greek symbols

ρ	density, kg/m^3
ρ_{fr}	density of frost, kg/m^3
δ_{fr}	frost thickness, *m*
ß	constant parameter used in calculation of frost thermal conductivity, *W.m2/kg.K*
e	heat exchanger effectiveness
t	time, *s*
?T	temperature difference, ^oC

Subscripts

a, air	air
acc	acceleration
act	actual
air	see ‘a’
amb	evaluated at store ambient air temperature
av	evaluated at average inlet and outlet conditions
c	tube outer surface, m
case	sum of radiation, lights and fan motor
comp	compressor

cyl	tube bank
Dc	tube collar diameter
Dh	hydraulic diameter
defrost	defrost
dis	evaluated at case discharge air temperature
dry	dry
duct	display case duct from coil exit to honeycomb (case discharge)
evap	evaporator
exit	coil exit
f,fin	fin
fan	evaporator fan
face	frontal (face) of heat exchanger
fr	frost surface
ht	height
in	inlet
inc	incremental (one time step)
ini	initial
l	liquid
lat	latent
len	length
max	maximum
metal	coil (fin plus tube)
0	before onset of frosting
o	overall (fin and tube)
out	outlet
r, ref	refrigerant
ret	evaluated at case return air temperature
s	saturated
sat	saturation
sens	sensible
si	base of the fin (i.e. tube outer surface)
sl	slot between fins
so	frost surface (fin or tube)
tb, tube	tube
th	thickness
total	total
tube	see tb
v	vapor
wall	wall
wd	width

Chapter 1: Introduction

1.1 Introduction

Frost accumulation is a direct result of the heat and mass transfer from the moist air passing over the cold heat exchanger surfaces. Whenever the temperature of the evaporator surface is below the dew point temperature, moisture in the air condenses. If the surface temperature is below freezing, frost begins to form.

Supermarkets account for ~4 % of the US electricity consumption with frozen and fresh food display cases representing most of the supermarket refrigeration load. Therefore it is essential to identify the ways in which frost buildup affects the efficiency of display cases. Then by exploiting the trade-offs among the underlying physical parameters, it is possible to reduce the impact of frost on the system performance.

Three frost related factors affect the rate of decrease in refrigerant evaporating temperatures (hence system efficiency): air flow blockage; change in air-side heat transfer coefficient; and the insulation effect of frost. Of these the reduction of air flow rate is most important because it degrades the air curtain, which separates the ambient (store) air from the refrigerated product. Deposition of frost on the evaporator coils increases the air-side pressure drop across the evaporator, ultimately decreasing the air flow rate and increasing the entrainment of warm and humid ambient (store) air. Frost affects the air-side heat transfer coefficient in two ways: reduction in air flow rate, reducing face velocity; and reduction in the free flow area which may increase the maximum velocity of air passing through the coil. The net increase or decrease in air-side heat transfer coefficient would then depend upon the dominance of these two opposing factors. Apart from air curtain degradation and change in air-side heat transfer coefficient, the frost deposited on the surface of the evaporator has very low thermal conductivity and insulates the cold surface from the warmer air. However, as more frost is deposited over time, its density and thermal conductivity increases, thus reducing its insulation effect.

1.2 Objective

This study focuses on development of a design tool (model) for simulating display case heat exchanger frosting and defrosting. The simulation model is then used to explore several design strategies: constant speed fan; variable speed fan; fin staging; and flat tubes with the objective to reduce defrost frequency and/or overall energy consumption of a supermarket display case. Once validated against standard experimental data, the model could provide a useful tool in developing design guidelines for a display case heat exchanger.

1.3 Literature review

This section provides a review of past research on experimental and analytical investigations of frost deposition on microscopic level as well as full-scale heat exchangers.

1.3.1 Frost properties

O'Neal and Tree (1985) provided a comprehensive review of frost research in simple geometries (flat plate, cylinders, tubes, parallel plates and annuli). Hoke et al. (2000) studied frost deposition on a variety of substrates at the microscopic level, and reviewed research on frost formation and growth. They observed frosting encountered on a refrigeration evaporator and characterized three distinct regimes: condensation period; early frost growth (layer grows at nearly constant rate); and mature growth period (frost grows proportional to the square root of time). Hayashi et al. (1976) reported that the early frost growth (crystal growth period) lasts only 2-5 minutes, followed by

frost layer growth period. The model proposed here therefore neglects the early crystal growth period and focuses on the problem of frost growth over many hours on full-scale heat exchangers. Only the mature frost growth period (layer growth) was modeled, assuming a negligible initial frost thickness (~0.02 mm) to avoid numerical discontinuities. Similar to Jones and Parker (1975), it was found that the initial frost thickness did not affect the model predictions at the subsequent time steps provided the initial thickness was small. Model simulations predicted ~0.02 mm of frost growth on heat exchanger surface during the first 2 min. of operation at conditions typical of refrigerated display cases.

1.3.2 Frost formation

Mao et al. (1999) correlated the frost thickness, density and conductivity as a function of environmental parameters, location on a flat plate, and Reynolds number, for conditions similar to those found in a freezer with the cold plate temperature from -20 ^{o}C to -41 ^{o}C, inlet air temperature from -10 ^{o}C to -26 ^{o}C and supply air velocities of 1 to 4 m/sec. They found that the frost characteristics differ significantly from those at room temperature air flow. For warmer plate temperature and lower supply air humidities the frost surface was characterized as smooth, thin and dense, while colder plate temperatures and high humidities gave rise to rough, thick and low-density frost.

Storey and Jacobi (1999) established a non-dimensional relation between frost thickness and square root of environmental time for frost formation on a flat plate, behavior that had also been observed in mature frost growth by Ostin and Andersson (1991). Their model captured the essential physics of mature frost growth and is a useful tool for data interpretation, but was based on data obtained when the frost surface temperature was close to freezing point.

Kondepudi and O'Neal (1987) provided a comprehensive review of the literature, detailing how frost growth degrades performance of heat exchangers. They reported that the wet fin efficiency (Sanders 1974) increases initially with frost growth and then tends toward a constant value. Meanwhile the overall heat transfer coefficient has an initial surge upon the onset of frosting (increased surface area and surface roughness), soon offset by the increase in the thermal resistance of the frost layer. Later, Kondepudi and O'Neal (1989) also investigated the frost growth effects on the performance of heat exchangers with flat and louvered fins.

Rite and Crawford (1990) studied the effects of frost on the UA value and air side pressure drop on a domestic refrigerator evaporator coil. They found that the UA value increases significantly as more frost forms on the evaporator under constant air flow conditions. They reported that the air flow rate affects the frosting rate due to its influence on mass transfer coefficient, evaporating surface temperature, and the moisture capacity of the air stream. The frosting rate was measured by observing the change in reservoir water height, assuming that all the water collected on the evaporator, and found it agreed within 15% with the weight gain of the frosted coil after the experiment.

Senshu et al. (1990) studied heat pump frosting on a two-row offset strip fin evaporator with a fin pitch of 2 mm at constant air flow rate. They documented that the mass transfer rate increases linearly with time and also it increases with decreasing the refrigerant temperature. As the air velocity decreases, frost formation rate increases. They also found that the air side heat transfer coefficient remained constant, but the air flow rate did not change during the experiments.

In a companion paper, Senshu et al. (1990) presented a heat pump frosting model and compared it to the experiments on a prototype heat pump system. In this model, they assumed a uniform smooth frost layer along the fin. A fan simulator model adjusted the air flow rate as frost formed on the evaporator. The simulation results agreed well with measured capacity, saturation temperature, air-side pressure drop, and outdoor air flow. However, the tests only lasted 40 minutes and no actual frost deposition patterns were reported.

Oskarsson, Krakow, and Lin (1990) tested a six-row heat pump evaporator outdoors under actual operating conditions with 315 fpm (8 fpi) and 12.7 mm (½") tubes and developed three computer models to simulate this heat exchanger. One was a finite element model, another was a three-region model, and the third was a parametric model. They were unable to fully validate these models during frosting against their experiments because they averaged their measurements over a long time period (half-hour intervals) and lacked control over the ambient conditions.

Kondepudi and O'Neal (1991) studied frosting on a single row, 9.5 mm (3/8") tube heat exchanger using an ethylene glycol-water mix. Wavy and corrugated fins were compared at 10 and 18 fpi; face velocity varied between 0.6 and 1 m/s, and relative humidity varied between 60 and 85%; and the experiments lasted 1 hour. Results showed how mass transfer increased with RH and fin density. Using a log mean enthalpy difference they calculated the overall energy transfer coefficient, E_o (W/m^2-K), observing that it stayed approximately constant because the air flow rate was held constant, increasing the local velocities over the frosted fins. The latent contribution to E_o was approximately 35 to 40%. Since this coil was only one row deep, they did not look at the frost distribution. The higher fin density caused air flow blockage to occur much sooner than in a commercial refrigeration heat exchanger.

Ameen (1993) conducted a series of 40-minutes long experiments on a heat pump evaporator that was 0.10 m (4") deep with 4 rows of 9.5 mm (3/8") tubes. Due to its relatively dense (but not quantified) fin spacing, the free flow area frosted up quickly, and the frost distribution across the heat exchanger was not studied.

Ogawa, Tanaka, and Takeshita (1993) studied ways to improve heat exchanger performance under frosting conditions, including staging, cutting, and/or extending the fins. They compared their experimental results to theoretical values. The theoretical values over predicted the experimental values of the average heat transfer coefficient and the average overall coefficient of heat transmission. Staggered fins, side staging, fin width extension, and partial cutting of fins just in front of the tubes all proved to be effective means of increasing the heat transfer rate.

Tassou and Datta (1999) studied frosting of multi-deck display case evaporator in a supermarket and in an environmental chamber. Their results quantified strong dependence of the defrost intervals on ambient humidity, because the principle source of moisture is air curtain entrainment. Air temperature measurements suggested that the evaporator became blocked with frost after 5 hours at a relative humidity of 50 %, 6.5 hours at 40 % RH, and 9 hours at 30 % RH when the ambient air temperature was 26 °C.

Itoh et al. (1996) studied frosting of one traditional and two other micro-channel evaporators "improved" with protruding fins, and compared them with a conventional round tube-flat fin evaporator. Within 20 minutes, the heat transfer rate on all three micro-channel evaporators decreased to less than half of the baseline value. They reported that the air-side configuration of the evaporator must be thoroughly modified before micro-channels can be used under frosting conditions.

Various researchers (Padki et. al. 1989, Rite and Crawford, 1990, Davis et. al. 1998) have found that frost deposition is initially favorable as it reduces fin-tube contact resistance and the rough frosted surface acts as fins, thus temporarily increasing the air-side heat transfer coefficient. However, as the frost thickens the insulating effect becomes dominant and the heat transfer rate is reduced. Also due to frost accumulation, the free flow area is reduced, thereby increasing the velocity of air and hence its heat transfer coefficient.

Carlson et al. (2001) focused on understanding how environmental conditions: air temperature and relative humidity; refrigerant temperature; and air and refrigerant temperature glide affect the deposition and distribution of frost on heat exchangers, typically of those found in refrigerated display cases. Experiments were conducted at 0 and -20 °C inlet air temperatures with relative humidity between 70 and 90 %, face velocities from 0.5 to 2.3 m/s, and refrigerant mass flow rates between 0.2 to 0.52 kg/sec. To minimize the uncertainty about the magnitude of the refrigerant side heat transfer coefficient, a single phase refrigerant, methoxy-nonafluorobutane (HFE), was used because it provides turbulent conditions even at low temperatures and flow rates. The objective was to gain a basic understanding of the effect of the operating conditions on the frost distribution, and to produce data of sufficient quality to support development and validation of a robust simulation model.

These objectives were met using several novel techniques. Dew point measurements at the entrance and exit of the heat exchanger were used to calculate the frosting rate as a function of time. The heat exchanger was suspended on a scale to enable real-time measurements of frost mass; this would not have been possible with a two-phase refrigerant because of void fraction variations. The measurement of the mass of water collected after defrosting provided a third independent determination of mass transfer. Pressure drop measurements were taken at four locations in the heat exchanger along the air flow direction to quantify the blockage effect of the frost. Finally, video cameras recorded frost deposition patterns from the top of the heat exchanger for different rows along air flow direction. Results demonstrated how frost forms under different operating conditions, and how frost may be distributed along the heat exchanger.

1.3.3 Model development

Numerous models have been developed to predict frost growth on simple geometries (e.g. single fin, flat plate etc.) as well as heat exchangers. Tao et al. (1993) developed a one-dimensional transient model of frost deposition on a cold surface exposed to warm moist air flow at about 20 ^{o}C. In the mature growth phase, the frost was modeled as a homogeneous porous medium with a distributed porosity and expanding boundary where diffusion was assumed to be the only mechanism for internal mass transport.

Padki et al. (1989) proposed a simple quasi-steady method of computing both the spatial and temporal variations of heat transfer, frost growth rate, frost thickness and surface temperature for a horizontal flat plate and a horizontal cylinder in both free and forced convection. Correlations relating frost density to the frost surface temperature (Hayashi et al. 1977) and frost conductivity to density (Sanders 1974 and Marinyuk 1980) were used and results were compared with published experimental data.

Chen et al. (2000 I & II) developed a more detailed numerical model to simulate frost growth on plate-fin heat exchangers for typical freezer conditions. Despite treating the frost layer as a one-dimensional transient porous medium, and using a two-dimensional transient heat conduction model for fins (frost properties vary over the fin

surfaces), their model could not predict the air-side pressure drop accurately when the frost blockage effects were large. Results were also very sensitive to the selection of correlations for calculating frost conductivity.

Oskarsson et al. (1990) presented heat pump evaporator models for operation with dry, wet and frosted surfaces. Senshu et al. (1990) and Kondepudi and O'Neal (1990) also considered the performance of heat pumps under frosting conditions. Sanders (1974) studied the frosting of air coolers.

Most of these studies focused either on frost properties on simple geometries (e.g. flat plate, horizontal cylinder) or frost-induced performance degradation of specific heat exchangers primarily heat pumps and air coolers. Moreover, the experiments were not designed for the purpose of developing and validating comprehensive models of frost growth over a wide range of operating conditions. Recently there have been more studies on ways to improve the performance of plate-fin-round-tube heat exchangers typically used for refrigerators and heat pump air conditioners under frosted conditions (Ogawa et al. 1993, Watters et al. 2002). Several methods including front staging, side staging and fin width extension were found to reduce the blockage effect at the leading edge and reduce air-side pressure drop.

However, little effort has been to model the effects of frost growth on supermarket display case heat exchanger performance and devise strategies to minimize such degradation. Verma et al. (2002) demonstrated development and validation of a simulation model (Wu et al. 2001) against Carlson's experiments for frost growth on full scale heat exchangers (typical of display case heat exchanger geometry) over a wide range of conditions. The parameter range for the experiments used to validate the model was: air supply temperature, 0 to -20 ^{o}C; inlet relative humidity, 70 to 90 %; face velocity, 0.6 to 0.9 m/sec; refrigerant inlet temperature, -10 to -30 ^{o}C; and refrigerant temperature glide, 3 to 5.5 ^{o}C. To facilitate validation, the model developed by Wu et al. (2001) was for indirect refrigeration and focused on air-side phenomena under constant running conditions i.e. steady inlet air and refrigerant temperatures and constant inlet relative humidity.

1.4 Display case heat exchanger model requirements

Open supermarket display cases commonly employ DX (direct expansion) evaporators and experience variable running conditions owing to increasing infiltration through the air curtain. Hence in order to gain an in depth insight into the mechanisms by which the frost degrades evaporator performance and develop strategies to minimize such degradation, the quasi-steady finite volume heat exchanger model developed and validated for secondary refrigerant was extended to simulate operation of open display cases, modeling the varying frost properties and operating conditions and their effects on heat exchangers with two-phase flow (i.e. primary refrigerant).

The model was further used to evaluate three design strategies: variable air flow operation; constant air flow operation; and fin staging to reduce defrost frequency and overall energy consumption of supermarket display cases. Identifying such design and operating conditions as fin staging, tube diameter, fin pitch and air flow rate, and exploiting tradeoffs among the aforesaid frost-related factors, it is possible to reduce the overall impact of frost deposition on system efficiency.

The model proposed requires certain geometry and operating condition parameters to simulate display case heat exchanger frosting and to determine defrost time and total energy consumption. The following parameters are assumed to be known:

1. Size and type of the case
2. Fan curve
3. Air entrainment fraction
4. Heat exchanger tube and fin geometry
5. Defrost performance

In order to simulate completely the performance of a particular display case it is necessary to include equations describing how the air curtain degrades as frost deposition changes the temperature and flow rate of the discharge air. This study focuses only on the heat exchangers and incorporates air curtain performance by using an experimentally determined expression for ambient air entrainment fraction as a function of air flow rate.

1.4.1 Size and type of the case

To simulate the performance of a particular type of a display case it is customary to know the size (length) of the case, whether it is 4', 6', 8', 12' or longer. It is essential to know the type of display case: low or medium temperature; vertical or horizontal or island; open or closed; single or multi-deck; self-contained.

1.4.2 Air flow rate

The initial rate of flow of air across the heat exchanger and its variation with pressure drop is calculated fromthe fan curve. The fan curve equations relate air flow rate to an increase in the air-side pressure drop as the heat exchanger geometry changes due to frost accumulation. The type of fan (SP, PSC or ECM), number of fans, fan motor and fan blade size and angle will determine the fan curve (pressure drop and power) for a particular case. For variable speed fans a family of curves is specified, to capture the effect of speed on motor efficiency.

1.4.3 Air entrainment fraction

Air entrainment fraction defines the percentage of the ambient (store) air that mixes with the display case discharge air and the mixed air then enters the return air duct. For the model it is essential to know the initial air entrainment fraction and its variation with air flow rate as frost accumulation reduces airflow. This fraction can be obtained for a particular air curtain from the variation of the case discharge and return air temperatures with time.

1.4.4 Heat exchanger coil and fin geometry

The coil type (round, flat, oval etc.) and size (diameter, length etc.), fin type (plain, wavy, corrugated), fin and tube spacing, and overall dimensions of the evaporator must be known in order to simulate the frosting and its effects for that heat exchanger geometry. Based on the type of heat exchanger geometry, the appropriate refrigerant-and- air-side heat transfer and pressure drop correlations must be incorporated as described in Chapter 2.

1.4.5 Defrost data

The mode of defrost, defrost initiation and termination criterion and fail safe time form the defrost data to be known beforehand to compute the defrost time and the load that it adds to the display case. Each of the four most commonly employed modes of defrost: electric; hot gas; timed off; and reversed air will have a different defrost initiation and termination criterion and fail safe time and hence a different effect on the optimal performance of the

heat exchanger under study. The fan operation schedule during defrost must also be known, as it will effect the product temperature during defrost.

Chapter 2: Numerical Model

2.1 Introduction

In order to study the effects of various parameters like air flow, inlet relative humidity, refrigerant inlet temperature, air inlet temperature on frost deposition and distribution, a heat exchanger frosting model was developed and validated (Verma et al. 2002) for a round tube-plain fin heat exchanger placed in a wind-tunnel. To facilitate validation, the model developed by Wu et al. (2001) was for indirect refrigeration and focused only on air-side phenomena under constant running conditions viz. steady inlet air and refrigerant temperature and constant inlet relative humidity. However open supermarket display cases commonly employ direct expansion (two phase) evaporators and experience variable running conditions owing to store air infiltration through the air curtain. Hence in order to gain an in depth insight into the mechanisms by which the frost degrades evaporator performance, develop strategies to minimize such degradation and estimate the optimal defrost frequency for a supermarket display case heat exchanger, the existing model has been extended to include the following:

1. DX operation (e.g. refrigerant temperature, pressure drop, and heat transfer coefficient etc.).
2. Mixing of store air with the display case air resulting in variable inlet relative humidity and air inlet temperature over time.
3. Fan curve to simulate variable air flow response to frost buildup on he heat exchanger.
4. Variable fin spacing and different package dimensions and coil geometry.

The model simulates R404A to investigate the heat exchanger performance for DX operation, and methoxy-nonafluorobutane (HFE), a single-phase refrigerant for indirect refrigeration.

Further, the DX version of the model developed incorporates Wattelet and Chato (1994) correlations (heat transfer coefficient) for two phase flow and Souza and Pimenta (1995) correlation for acceleration and frictional pressure drop. Certain assumptions have been made for the development of the model, they are:

1. A quasi-steady finite volume approach is used to analyze the transient heat exchanger performance whereby calculations at one time step are used for analysis at the next time step.
2. Heat exchanger surface is modeled for mature frost growth by assuming that there exists a finite (negligible) amount of frost on the surface of the heat exchanger even before the start of the operation. This assumption avoids the complexity in modeling the early stages of frost growth, namely, the crystal growth period.
3. The effect of surface roughness of the frost is neglected. Note that frost surface is initially rough and uneven due to the random nature of the deposition of frost. The roughness and actual surface area of the frost surface are usually difficult to predict. It might contribute to an enhancement of the heat transfer to the heat exchanger. But as Sanders (1974) has found, the surface roughness effect of enhancing the heat transfer has a significant effect only in the early stages of frost formation. Later the insulation effect makes it inconsequential. Since our model usually describes a long period of frosting on a full-scale heat exchanger, most of the time should be outside the early stage of frost formation. Therefore surface roughness is not considered in the model.
4. The frost is evenly distributed on the surface of the tubes and fins in each tube row (finite volume).
5. The heat exchanger has a cross-counter flow arrangement with warmest inlet air coming in contact with the refrigerant exiting the heat exchanger.
6. The refrigerant leaves the condenser in a saturated liquid state at a condensing temperature of 40 ^{o}C.
7. At the exit of the heat exchanger the refrigerant is superheated by 1.5 ^{o}C. This is obtained by having almost single phase flow (saturated/superheated) in the first tube row along air flow direction.

8. When the frost surface temperature reaches the freezing point, the density of the frost can be linearly extrapolated until it rises to the density of ice at 0 ^{o}C (920 kg/m^{3}) while the thickness of the frost remains constant. Once the density of frost reaches the ice density, the thickness of the frost increases while the density of the frost remains constant. For more details see Sec. 2.3.9.

2.2 Quasi-steady finite volume approach

In order to simulate the frost deposition patterns, the heat exchanger was divided into certain number of finite volumes, shown with dotted lines in Figure 2.1, along the air flow direction. Each finite volume comprises a row of tube banks transverse to the air flow direction. The exit of one finite volume formed the inlet of the next finite volume and so on. Transient performance was approximated by a quasi-steady process where calculations at one time step served as inputs for the next as shown in Figure 2.2. The results from one time step (i.e. frost thickness) were used to update the heat exchanger geometry (fin thickness, tube diameter) for the next time step. The time interval used in the model was three minutes. Simulations under frosted conditions typically lasted for ~4-5 hours. Carlson's experiments revealed that the three- minute time increment yielded solutions within 1 % of the one-minute increment at all operating conditions.

To start the quasi-steady simulations it was necessary to assume initial values for frost thickness (0.2 mm) and frost density (40 kg/m^{3}). Results after the second time step were insensitive to these initial values.

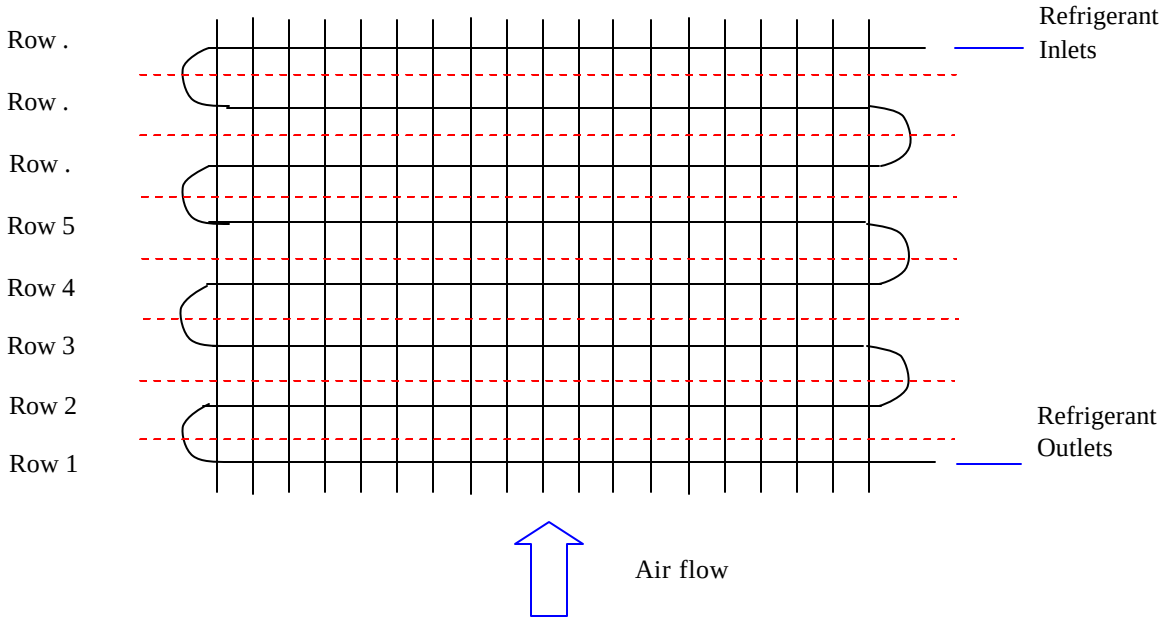

Figure 2.1 Top view of the heat exchanger

2.3 Numerical model

Figure 2.2 depicts the structure of the simulation model. At each time step the input parameters (air and refrigerant inlet temperature, air flow, inlet relative humidity and mass flow rate of refrigerant) along with the geometry (tube diameter and fin spacing) and air and refrigerant side heat transfer and pressure drop are solved for the sensible, latent and total loads, air and refrigerant exit temperature and pressure, frost inner and outer surface temperature and incremental frost mass deposited using the heat and mass transfer governing equations. Depending upon the frost surface temperature the density of incremental frost deposited at this time step was determined using the Hayashi's (1976) correlation if the frost surface temperature is below freezing point and linear extrapolation to

density of ice at freezing point (i.e. 920 kg/m^3) otherwise (i.e. $T_{so} = 0$). Yonko and Sepsy (1967) correlation is used to determine the frost conductivity as a function of frost density (already been computed). Finally from all the determined parameters the heat exchanger geometry is updated for tube diameter and fin thickness for each finite volume depending upon the incremental frost thickness for that particular finite volume.

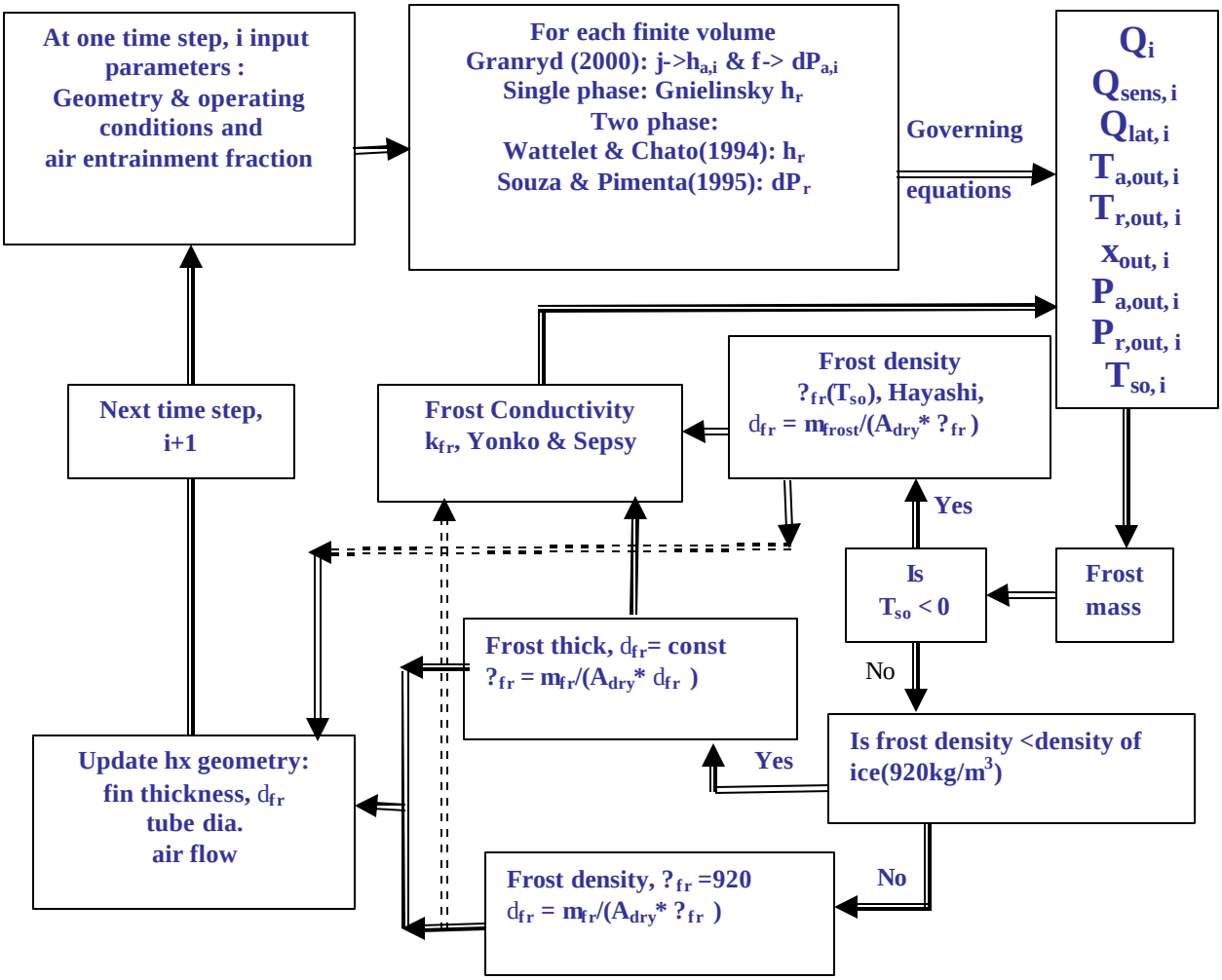

Figure 2.2 Structure of the model

2.3.1 Air-side heat transfer coefficient

While most of the heat transfer correlations (Kim and Webb 1999, Wang and Chang 1998, Wang et al. 1996) have been developed for a wide range of Reynolds number, fin pitch, tube diameter and tube spacings, there exists no correlation to predict the heat transfer coefficient for a multi-row (more than 6 rows of refrigerant circuits) heat exchanger with variable fin pitch. Kim and Webb's (1999) heat transfer correlation (given in Appendix A) developed for a multi-row heat exchanger assumed that the heat transfer coefficients of the coils having more than three coils to be negligibly different from that of three row coil. They conducted experiments for dry coils with the fin spacing being constant. However in our model the fin spacing varies after the first time step even though it is constant to start with. This is due to the uneven frost distribution across the heat exchanger due to varying driving

potential (humidity difference) for frost deposition along the air flow direction. Further if a heat transfer correlation developed for a single row is used then the turbulence produced by the upwind tubes goes neglected.

Using the experimental data obtained from one of the leading supermarket display case manufacturers, the heat transfer coefficient determined using Kim and Webb (1999) correlation was compared to that backed out from the experimental observations and it was found that Kim and Webb's correlation over predicts the heat transfer coefficient backed out from experimental data provided by as much as 50%.

The model was developed with the intention to explore a wide range of heat exchanger geometries, and j and f-factor correlations of Wang et al. (2000) were based on the largest and most diverse sets of data. Non-dimensionally the parameters describing typical display case evaporators lay barely within the parameter space of the correlation. However in absolute terms, both tube diameter and fin spacing lay outside the range of the correlation. The pitfalls become obvious when examining the friction factor correlation which increased monotonically with fin pitch for typical tubes dimensions (11 mm OD) and fin pitch ~8.5 mm – obviously an incorrect representation.

Granryd et al. (1999) developed a correlation for air-side heat transfer and pressure drop for plain fin-round tube heat exchangers with tube diameter, transverse and longitudinal tube spacing, and fin spacing typical of commercial and industrial and residential applications under dry conditions. His correlation was based on a series of experiments with electrically heated copper plates simulating the fins, and cylindrical or oval pieces of brass simulating the tubes. The heat transfer to the cylinders was calculated as for a bundle of smooth tubes by the method of Grimson (1937) described in Granryd et al. (1999). The influence of the tubes and of the fin spacing on the heat transfer to the fins was taken into account by introducing a factor C_h to be multiplied by the coefficient of heat transfer of a narrow slot without tubes. The dependence of the coil depth was simulated by the introduction of another factor k_z. This leads to the following expression for the mean heat transfer coefficient of the total area.

$$h_a = K_z \cdot \left(h_{a,cyl} \cdot \frac{A_{a,tb}}{A_{a,total}} + C_h \cdot h_{a,slot} \cdot \left(1 - \frac{A_{a,tb}}{A_{a,total}} \right) \right) \qquad (2.1)$$

The parameters/terms used in the above equation along with their computation are listed in Appendix A.

Appendix B compares three air-side heat transfer correlations: Granryd et al. (1999); Wang et al. (2000); and Kim et al. (1999) collectively spanning a wide range of data. Based on the range of these correlations, two medium temperature display case heat exchanger geometries and experimental results, Carlson's experimental results, and the effect of varying fin pitch and air flow rate on the predicted air-side heat transfer coefficient, the selection was narrowed down to using Granryd's correlation for air-side heat transfer coefficient.

2.3.2 Air side pressure drop

For air-side pressure drop the three correlations: Kim et al. (1999); Wang et al. (2000); and Granryd et al. (1999) were considered. Based on criteria similar to air-side heat transfer coefficient, Granryd's air-side pressure drop correlation was chosen to be used in the model. Details can be found in Appendix B.

Granryd's correlation was based on pressure drop for narrow slots without tubes and then it was combined with equations for the pressure drop in tube bundles. The influence of the tubes on the pressure drop of the fins was

considered by the introduction of additional parameters and the final correlation was given by the following equation.

$$dP_a = z.P_z.\left(\frac{r.V_{sl}^{\ 2}}{2}\right)\left(V_{1,2} + z_r.V_r + \frac{C_f.f_{sl}.L}{2.Fs}\right) \qquad (2.2)$$

The parameters/terms used in the above equation along with their computation are listed in Appendix A.

2.3.3 Frosted fin and tube analysis

Though many efforts have been devoted to study of fin surface efficiency under dehumidifying conditions, the available literature on frosted heat exchangers still offers very limited information. The wet fin surface efficiency used by various authors (Threlkeld 1970, Sanders 1974) is determined by the analysis of the fin with the total thermal resistance offered due to convection (from air) and conduction (within water/ frost). However, this analysis eliminates the frost/ water surface temperature from consideration. We treat it explicitly in our model because it determines the frost density and hence its conductivity. The thickness of frost depends on these two frost properties.

The essence of the model is to determine the frost surface temperature by solving simultaneously the separate equations for the convective heat (sensible) and mass (latent) transfer between ambient air and the frost surface. The combined sensible and latent heat transfer i.e. the total heat transfer is analyzed for conduction within the frost layer.

Wu et al. (2001) defined frosted fin conduction efficiency by analyzing a frosted fin for conduction from frost surface to fin surface and conduction from fin tip to fin base. By setting up the heat balance for a fin element, a frosted fin parameter (equivalent to fin parameter for dry fin analysis) was determined and the frosted fin efficiency was based on it. However their analysis neglected the conduction within the frost layer from frost tip to fin base and also assumed the surface temperature of frost on tubes and fins to be the same (hence same thickness of frost on tubes as well as fins) within each finite volume. When the frost is thin, the heat transfer from frost to base is negligible in comparison to the heat transfer from fin to base. However as shown in Appendix C the conduction along the frost to the base accounts for as much as 26 % with ~2 mm of frost being deposited on the surface of the fin.

A totally different but physically viable analysis of the frosted fin was implemented in this model. Both the conduction heat transfers namely, from frost directly to fin base; and from frost surface to the fin and then along the fin to the fin base were analyzed by assuming one, two and three lump models of homogenous frost and fin masses. Also the frost on the surface of tubes was considered separately than that on fin surface. It was found frost surface and fin temperatures for single lump models were slightly lower than the respective average values for two-and three-lump models. However the two-and three-lump models agreed within 1 %, so the two-lump model was implemented in the model. For more details refer to Appendix C.

2.3.4 Refrigerant side heat transfer coefficient

The refrigerant side heat transfer coefficient was determined based on the state of the refrigerant. For tubes with refrigerant in single phase flow (saturated or superheated), Gnielinski's (1976) correlation for fully developed turbulent flow in a circular tube was used while for two phase flow with quality less than 85 % Wattelet and Chato (1994) correlation was utilized. For near saturated refrigerant (with more than 85 % quality), a linear interpolation

between Wattelet and Chato (1994) and Gnielinski (1976) was utilized to determine the refrigerant side heat transfer coefficient. For details of correlations see Appendix A.

2.3.5 Refrigerant side pressure drop

For tubes with two phase refrigerant flow the Souza and Pimenta (1995) correlation was used to determine the refrigerant frictional and acceleration pressure drop. The total refrigerant pressure drop was given by

$$dP_{ref} = dP_{friction} + dP_{acc} \tag{2.3}$$

The frictional pressure drop, $dP_{friction}$ was determined from the following equation

$$dP_{frition} = \frac{f * G_{ref}{}^2 * \frac{L}{d_i} * v_l * j}{2000} KPa \tag{2.4}$$

where,

f = two phase multiplier

And the acceleration pressure drop was given by

$$dP_{acc.} = \frac{G_{ref}{}^2 (|A_{12}| - |A_{11}|)}{1000} KPa \tag{2.5}$$

where,

$$A_{11} = \frac{x_{in}{}^2 * v_v}{raf_{in}} + \frac{(1 - x_{in})^2 * v_l}{(1 - raf_{in})} \tag{2.6}$$

$$A_{12} = \frac{x_{out}{}^2 * v_v}{raf_{out}} + \frac{(1 - x_{out})^2 * v_l}{(1 - raf_{out})} \tag{2.7}$$

For refrigerant side friction factor, void fraction and two phase multiplier computations see Appendix A.

For single phase flow the refrigerant side pressure drop was determined using the following relation,

$$dP_{ref} = \frac{f * G_{ref}{}^2 * \frac{L}{d_i} * v_v}{2000} \tag{2.8}$$

Here Darcy's friction factor based on Churchill's (1977) correlation was used for transition/ turbulent flow (given in Appendix A) while for laminar flow the friction factor was determined from the following relation,

$$f = \frac{64}{\mathrm{Re}} \tag{2.9}$$

2.3.6 Air entrainment fraction

Air entrainment fraction is defined as the percentage of ambient air that gets mixed with the display case discharge air and goes into the return air duct. Based on experimental data obtained from display case manufacturers, the variation of the air entrainment fraction (af) could be expressed as a function of air flow rate (shown in Chapter 3). The relationship is actually much more complex, but this simple expression is assumed to adequate for the single design operating condition considered here. This infiltration load combined with other case

loads (shown in Figure 2.3) such as lights, radiation, and fans was used to calculate the evaporator air inlet (return air) state.

$$(1\text{-}af).\dot{m}_{air}.h_{dis} + af.\dot{m}_{air}.h_{amb} + Q_{case} = \dot{m}_{air}.h_{ret} \quad (2.10)$$

$$(1\text{-}af).w_{dis} + af.w_{amb} = w_{ret} \quad (2.11)$$

Then typical values for variation of this air entrainment fraction with air flow rate were incorporated in the model to simulate the variation of return air temperature and return air humidity with time i.e. variable operating conditions.

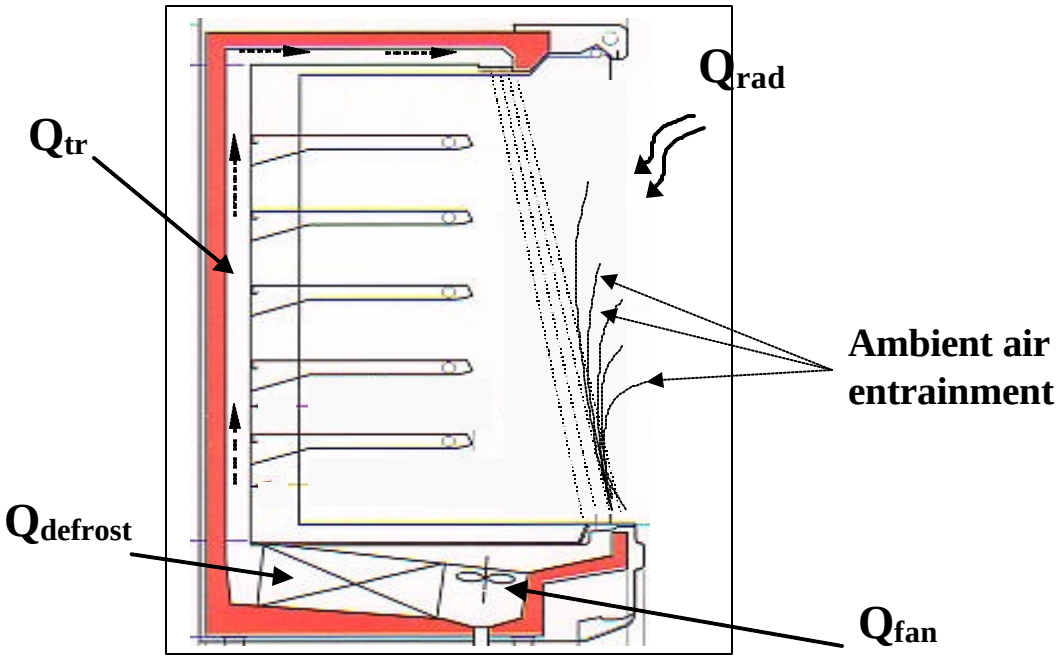

Figure 2.3 Loads on a supermarket display case evaporator (open)

2.3.7 Fan curve

In order to effectively investigate the effects of frost growth on heat exchanger it is extremely important to simulate the variation in air flow rate due to an increase in the airside pressure drop with an increase in frost growth. This is accomplished by including the fan curve (relation between the air-side pressure drop across fan with the air flow rate) in the model simulations. There are numerous types of fans with different blade diameters and blade angles and fan motors (SP, PSC, ECM etc.). For our model simulations we assumed fans typical of a medium temperature meat merchandiser running in parallel, driving the air across the display case heat exchanger, and producing the desired air curtain. One such fan curve is presented in Chapter 3. The pressure drop across the fan under actual operating conditions is then calculated from the fan curve (at standard operating conditions) as:

$$dP_{fan,act} = dP_{fan,curve}\frac{r_{act}}{r_{std}} \quad (2.12)$$

where,

$?_{std}$ = density of air at standard operating conditions, ~21 ^{o}C (70 ^{o}F), kg/m^{3}

$?_{act}$ = density of air at actual operating conditions, kg/m^3

The pressure drop across the duct at the start of simulation was backed out from the pressure drop across fan at the start of simulation using the initial air flow rate obtained from a display case manufacturer i.e.

$$dP_{duct,ini} = dP_{fan,ini} - dP_{evap,dry} \tag{2.13}$$

For further simulations the changes in the pressure drop across the duct was determined from the fan laws using the dry pressure drop across duct defined above and subsequent changes in the air flow rate and density of air.

$$dP_{duct} = dP_{duct,ini}\left(\frac{\dot{V}_{air}}{\dot{V}_{air,ini}}\right)^2\left(\frac{r_{air,exit}}{r_{air,ini}}\right) \tag{2.14}$$

where,

$V_{air,ini}$ and $\rho_{air,ini}$ = air flow rate (m^3/s) and density of air respectively, at the start of simulation, and

$\rho_{air,exit}$ = density of air at the exit of the coil

Now, the pressure drop across the heat exchanger during simulations (using Granryd et al. 1999 correlation), pressure drop across the fan (from fan curve) and pressure drop across the duct given by Eq. X.13 are used to calculate the air flow rate across the coil i.e.

$$dP_{fan} = dP_{evap} + dP_{duct} \tag{2.15}$$

2.3.8 Heat and mass transfer.

The mass transfer rate was calculated by solving simultaneously the continuity one-dimensional mass transfer equations for fins and tubes separately for each of the finite volumes, using the heat and mass transfer analogy given by Eq. 3

$$\dot{m}_{fr} = \dot{m}_{air}(w_{in} - w_{out}) \tag{2.16}$$

$$\dot{m}_{fr} = (h_a \cdot Le^{-2/3} / c_{p,a}) \cdot A_o \cdot (w_{av} - w_{so}) \tag{2.17}$$

These equations determined the frosting rate, $\dot{m}_{fr}$ and the air outlet humidity, w_{out}.

Figure 2.4 shows a fin and tube surface covered with frost. Since the heat exchanger has already been divided into several finite volumes, the arithmetic mean temperature of air (T_{av}) was used for computation of one-dimensional sensible heat transfer (fins and tubes separately) for each segment, which is driven by the temperature gradient between the air and frost surface. For each finite volume it was solved simultaneously with the air-side energy balance for known values of air inlet temperature, air-side surface area and air mass flow rate. The surface temperature of the frost on fins and tubes was computed separately within each finite volume. The frost surface temperature on the tubes would be slightly lower than the frost surface temperature on the fins. Latent heat transfer resulted from the formation of frost on the surface of tubes and fins. The total heat transfer (sum of fin plus tube heat transfer) was determined by solving simultaneously the equations for conduction through the frost layer (tubes plus

fins), heat transfer from the tube to refrigerant and refrigerant-side energy balance. Refer to Appendix C for details on conduction heat transfer through the frost layer on the surface of fin.

$$Q_{sens,fin} = h_a \cdot A_{fin}\left(T_{a,av} - T_{so,f}\right) \tag{2.18}$$

$$Q_{sens,tube} = h_a \cdot A_{tube}\left(T_{a,av} - T_{so,tb}\right) \tag{2.19}$$

$$Q_{sens} = Q_{sens,fin} + Q_{sens,tube} \tag{2.20}$$

$$Q_{sens} = \dot{m}_{air}\, c_{p,a}(T_{a,in} - T_{a,out}) \tag{2.21}$$

$$Q_{lat,fin} = \dot{m}_{fr,f}\, h_{sg} \tag{2.22}$$

$$Q_{lat,tube} = \dot{m}_{fr,tb}\, h_{sg} \tag{2.23}$$

$$Q_{lat} = Q_{lat,fin} + Q_{lat,tube} \tag{2.24}$$

$$Q_{fin} = Q_{sens,fin} + Q_{lat,fin} \tag{2.25}$$

$$Q_{tube} = Q_{sens,tube} + Q_{lat,tube} \tag{2.26}$$

$$Q_{fr,fin} = Q_{fin,si} \tag{2.27}$$

$$\mathrm{Q_{fin}} = \mathrm{Q_{fr,si}} + \mathrm{Q_{fin,si}} \tag{2.28}$$

$$\mathrm{Q_{tube}} = \mathrm{k_{fr,tube}}.2.\mathrm{N_{tube}}.\boldsymbol{p}.\left(\mathrm{W} - \mathrm{N_{fin}}.\mathrm{f_{th}}\right).\frac{\left(\mathrm{T_{so,tube}} - \mathrm{T_{si}}\right)}{\left(\ln\left(\frac{\mathrm{Dc}}{\mathrm{Dc_0}}\right)\right)} \tag{2.29}$$

$$Q_{total} = Q_{fin} + Q_{tube} \tag{2.30}$$

$$Q_{total} = h_{ref} \cdot A_r\left(T_{si} - T_{r,av}\right) \tag{2.31}$$

$$Q_{total} = Q_{sens} + Q_{latent} = \dot{m}_{ref}\, c_{p,r}(T_{r,in} - T_{r,out}) \tag{2.32}$$

The heat and mass transfer governing equations, together with the refrigerant and air-side heat transfer and pressure drop correlations described before, were solved simultaneously for frost surface temperature, frosting rate, and air and refrigerant outlet temperatures. The fin and tube incremental frost mass (frost mass for one time interval) thus determined separately was used to calculate separately, the fin and tube incremental frost thickness using the Hayashi's correlation or linear interpolation to density of ice as explained in section 2.3.9 below. This incremental frost was then added to the frost layer already existing on the fin and tube surfaces. Finally the density of frost (hence conductivity) on fins and tubes to be used for the next time step was computed using the existing frost thickness (after the addition of incremental frost) and total amount of frost deposited (after addition of incremental frost mass).

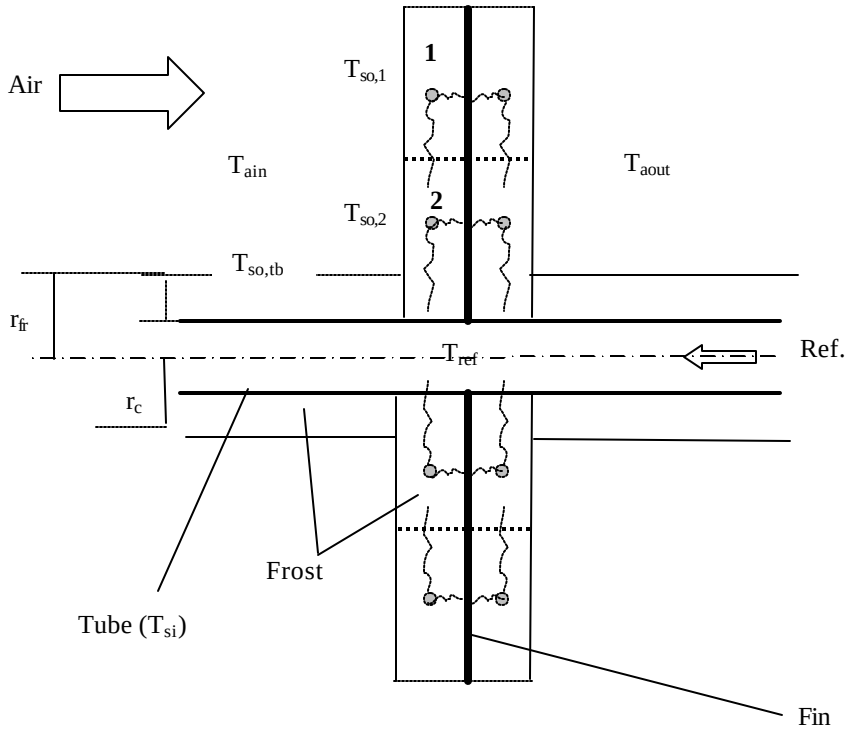

Figure 2.4 Heat transfer from the air through the frost layer, tube and fin to the refrigerant

2.3.9 Frost thickness and density

(i) Frost thickness

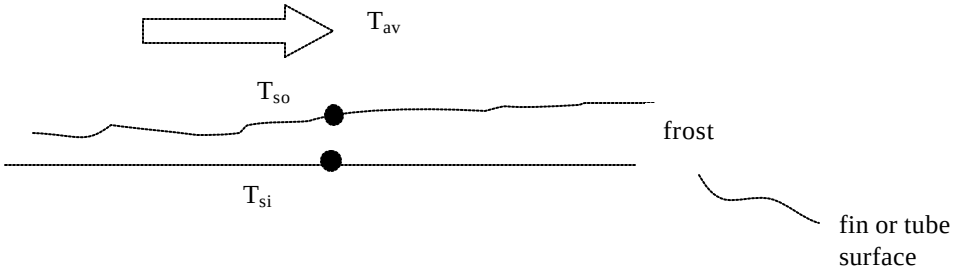

Figure 2.5 Single fin (or tube) frosting

Figure 2.5 shows the model for determining the frost thickness and density. Here it is assumed that the changes in the frost density along the thickness of the frost (from base to surface) are negligible. In the model, T_{si} (base temperature of the fin) is determined after considering the surface efficiency of the frosted fin, while T_{so}, the surface temperature of the frost is used to determine the frost density for temperatures below freezing. The frost on the surface of the tubes and fins is accounted for separately by solving for the respective frost surface temperatures using the conduction heat transfer.

The incremental thickness of the frost layer on the surface of the fin (and tube) is computed by dividing the incremental mass of frost accumulated (frost mass for that time interval) on fins (and tubes) by the product of incremental density (based on the current frost surface temperature) of frost on fin (and tube) and surface area of fin (and tube) under dry operating conditions.

$$d_{fr,fin,inc} = \frac{m_{frost,fin}}{r_{fr,fin,inc} \cdot A_{fin,dry}} \tag{2.33}$$

(ii) Frost density

Hayashi's (1976) empirical correlation is used to determine frost density when the frost surface temperature is below freezing.

$$r_{fr} = 650e^{0.277 T_{so}} \tag{2.34}$$

The limitation of this empirical correlation arises when the frost surface temperatures fall below -10 ^{o}C as seen in Figure 2.6 which depicts Eq. (2.34). However, Chen (2000) measured frost characteristics on heat exchanger fins for typical freezer operating conditions with base temperatures form -31 to -38 ^{o}C and air supply temperatures from -13 to -21 ^{o}C and found that the frost density varied from 100 to 145 kg/m^3 along the air flow direction for air supply temperature of -15 ^{o}C and plate temperatures of -35 ^{o}C. Due to scarcity in the literature about the density of frost at lower surface temperatures (below -25 ^{o}C), a constant frost density of 130 kg/m^3 is used for the analysis of such cases.

Another limitation of this correlation arises when the frost surface temperature rises to freezing temperature (0^{o}C) or higher during the running period, for a particular finite volume. In such a case there is an occurrence of repeated cycles of melting and refreezing once the frost surface temperature reaches the freezing point. Raju (1993) explains the consequence of this effect, which causes structural changes in the frost layer that tend to increase both the density and thermal conductivity of frost. This phenomenon is more likely to occur in cases with high-humidity and/or high-temperature environments than the low-humidity and low-temperature ones. Since this mechanism is not captured in the correlations for frost density and conductivity, we did not include it in this model. Moreover, the potential for this problem to occur is limited to the high-temperature and high-humidity simulations and then only in the first (usually superheated) tube row where the thickness of the frost was much less (4 times) than the other finite volumes of the heat exchanger.

For any finite volume where the frost surface temperature reaches the freezing point, the model assumes that the frost density would ultimately reach the density of ice at the freezing point, with the water continuously seeping into the porous frost layer increasing its density and the frost thickness remains constant (i.e. no incremental frost thickness). Once the frost density reaches the density of ice (920 kg/m^3), it is held constant while the frost thickness increases (i.e. incremental frost being deposited at density of ice) with further mass transfer. For finite volumes where the frost surface temperature is below the freezing point Hayashi's correlation is successfully applied.

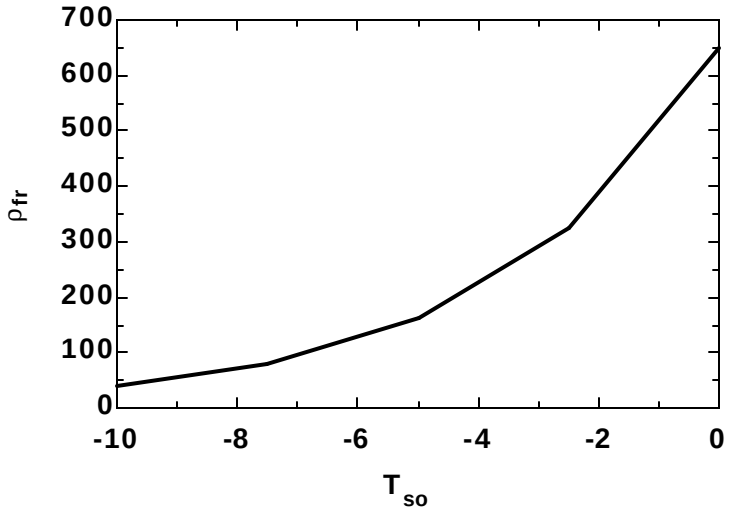

Figure 2.6 Variation of frost density with surface temperature, Hayashi (1976)

2.3.10 Frost conductivity

The thermal conductivity of frost was determined by employing the Yonko and Sepsy (1967) correlation between the frost conductivity and frost density. The relation is generally of the form: $k_{fr} = k_0 + b \cdot r_{fr}$.

The Yonko and Sepsy correlation to determine frost conductivity is

$$k_{fr} = (0.02422 + 7.214 \cdot 10^{-4} \cdot r_{fr} + 1.1797 \cdot 10^{-6} \cdot r_{fr}^{\,2})/1000 \qquad (2.35)$$

This equation implies that β = $7.214 \times 10^{-4} W \cdot m^2 / kg \cdot K$. We assume it to be constant. Actually, β= 7.214×10^{-4} (1 + r_{fr}), which means β should vary with r_{fr}. However, there will be only 0.1 % change in β for our entire range of frost density (130 ~650 kg/m^3) predicted by the model.

Yonko and Sepsy (1967) also tested a wide range of frost surface temperature from -30^{o}C to –5.7 ^{o}C, which is very similar to our surface temperature and their correlation is limited to r_{fr} < 576 kg/m^3. However their correlation when extrapolated to the density of ice predicts the thermal conductivity of ice within 10 % of the tabulated values as shown in Figure (2.7) below.

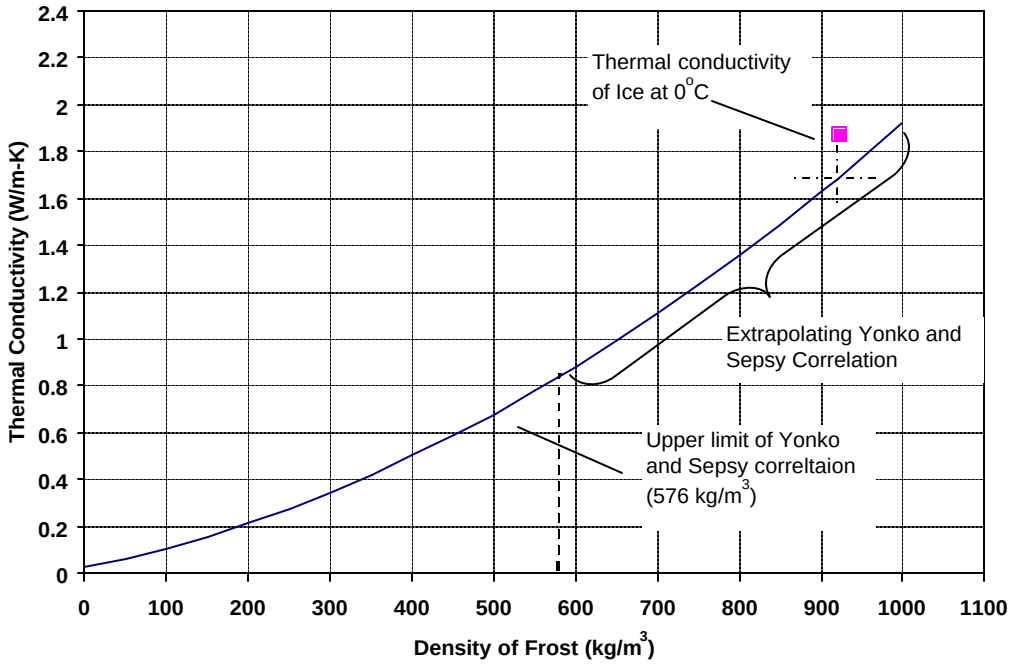

Figure 2.7 Yonko and Sepsy frost thermal conductivity correlation (1976)

2.4 Defrost time and compressor and fan energy consumption

2.4.1 Defrost time

Since the frost deposition on heat exchanger surfaces reduces the air flow rate (rise in pressure drop), defrosting becomes essential once the air flow rate falls below the design air flow rate. The defrost energy consumption would depend on the mode of defrost (electric; hot gas; off time; and reversed air), defrost initiation and termination criterion. Each mode of defrost would have a different effect on the optimal performance of the heat exchanger under study. In the model, off time defrost (fans running and no refrigerant flow) was used to incorporate defrost energy consumption because it is the most common method of defrosting medium temperature open display cases. The energy required to melt the frost comes from the warm store (ambient) air circulated by the fan over the frosted heat exchanger surfaces.

Few assumptions were made to include the defrost energy requirements in the model:

1. The heat transfer coefficient of the air flowing over the coils is taken as the average value of the unfrosted and fully frosted coil.
2. Entire heat exchanger surface is at the ambient temperature at the end of defrost i.e. before the start of frosting simulations.
3. Defrost termination criterion was chosen to be the time when all the frost has melted.
4. The energy required to raise temperature of frost (actual frost temperature ~ -5 ^{o}C) to the freezing point was neglected in comparison to that required to melt frost and to raise the temperature of the entire heat exchanger metal to the ambient temperature.
5. To ensure the removal of entire frost existing on all heat exchanger surfaces, the ideal defrost time (described in the governing equations) was multiplied by a fail safe factor of 2.3. This resulting time agreed with the manufacturer's total defrost time (including fail safe time) specified time in the catalog. This was essential so that during defrosting the non-uniform air flow over the heat

exchanger surfaces does not result in some frost being retained at some locations at the end of defrost resulting in more and more frost accumulating at those locations during successive cycles.

6. The fail safe time resulted in entire heat exchanger surface to be at the ambient temperature.

2.4.2 Governing equations:

The defrost time is calculated (Eq. 1) from the total amount of frost deposited at the end of one run time (one frosting period) and melting rate of frost. This melting rate was determined using Eq. 2 by solving for the air-side energy balance (determined using ε-NTU approach, Eq. 3-5) together with the energy required to melt the frost (Eq. 6) and raise the temperature of the heat exchanger metal (Eq. 7) to the ambient temperature.

$$t_{defrost} = \frac{m_{fr}}{\dot{m}_{melt}.3600} \tag{2.36}$$

$$\dot{Q}_{defrost} = \dot{Q}_{frost} + E_{metal} / t_{defrost} \tag{2.37}$$

$$\dot{Q}_{defrost} = \dot{Q}_{\max}.e \tag{2.38}$$

$$\dot{Q}_{\max} = h_{air,av} A_o.\Delta T_{fr} \tag{2.39}$$

$$\Delta T_{fr} = T_{amb} - 0 \tag{2.40}$$

$$\dot{Q}_{frost} = \dot{m}_{melt}.h_{f,melting} \tag{2.41}$$

$$E_{metal} = m_{metal}.c_{p,metal}\Delta T_{metal} \tag{2.42}$$

$$\Delta T_{metal} = T_{amb} - T_{metal,ini} \tag{2.43}$$

2.4.3 Compressor and fan energy consumption

With the defrost time known, the compressor energy requirement (kW.hr/day) was determined using the compressor power map and the total time in a day the compressor is in operation (Eq. 9). Since timed-off mode of defrost was used, the fans were running all the time (frosting and defrosting) and the fan energy requirement was determined by the average fan power (using fan curve) spread over 24 hours. The total energy requirement (fan plus compressor) for a day was calculated as the sum of the compressor and fan energy requirements. The COP of the system can then be defined as the ratio of the total refrigeration effect produced during frosting to the total energy requirements.

$$E_{comp} = \dot{W}_{comp}.(24 - t_{defrost}) \tag{2.44}$$

$$E_{fan} = \dot{W}_{fan}.24 \tag{2.45}$$

$$E_{total} = E_{comp} + E_{fan} \tag{2.46}$$

Chapter 3: Evaluation of Design Strategies

Two design strategies for reducing defrost frequency and overall energy consumption of open supermarket display cases were evaluated relative to the baseline (variable air flow as a consequence of fan characteristics) operation: constant air flow operation; and fin staging. An experimentally validated simulation model for a secondary refrigerant was extended to simulate operation of open display cases (details in Chapter 2), modeling the varying frost properties and operating conditions and their effect on heat exchanger performance.

3.1 Evaluation of design strategies

To illustrate the capabilities of the simulation model, several strategies for decreasing defrost frequency were explored. Recall that frost deposition on the evaporator surface reduces the air flow rate due to an increase in the air-side pressure drop, insulates the air from the evaporator surface and alters the air-side heat transfer coefficient. There is significant potential to minimize adverse impacts through optimal selection of design parameters (e.g. fin spacing, fin thickness, tube diameter, package dimensions) and operating variables (e.g. air flow rate, evaporating temperature, refrigerant mass flow rate, return air temperature and humidity).

For open display cases where air curtain integrity defines the criterion for defrost initiation, most design and operating parameters are fixed due to geometrical constraints and/or case ambient (store air) conditions. The following analysis assumes that the overall package dimensions of the evaporator are fixed due to the size of the display case, and the return air temperature and humidity are determined by the entrainment of the store air.

3.1.1 Variable air flow (baseline operation)

To understand the mechanisms by which frost degrades evaporator performance, an 11 row (44 passes in 4 refrigerant circuits) 2.44 m (8 ft.) medium-temperature open display case evaporator (2^{o}C superheat) equipped with four fans running in parallel was considered. For our model simulations we assumed four fans (GE 5KSM51ECG3799, typical of a medium temperature meat merchandiser) were running in parallel driving the air across the display case heat exchanger and producing the desired air curtain. The fan curve for the above fan is depicted in Figure 3.1 and the relationship between the pressure drop across four fans running in parallel and the volumetric air flow rate across heat exchanger is expressed by eq. (3.1). Simulations quantified the air-side pressure drop, hence the reduction of air flow rate via the fan curve, on evaporator capacity and defrost interval. The air entrainment fraction (expressed as a function of air flow rate) given by Eq. 3.2 was determined from the manufacturer data for variations over time of return and discharge air temperatures.

$$dP_{fan} = -9.98.\ \dot{V}_{air}{}^{2} - 115.\ \dot{V}_{air} + 81.14. \tag{3.1}$$

$$af = 0.783 - 1.66*10^{-3} cfm + 1.16*10^{-6} cfm^{2} \tag{3.2}$$

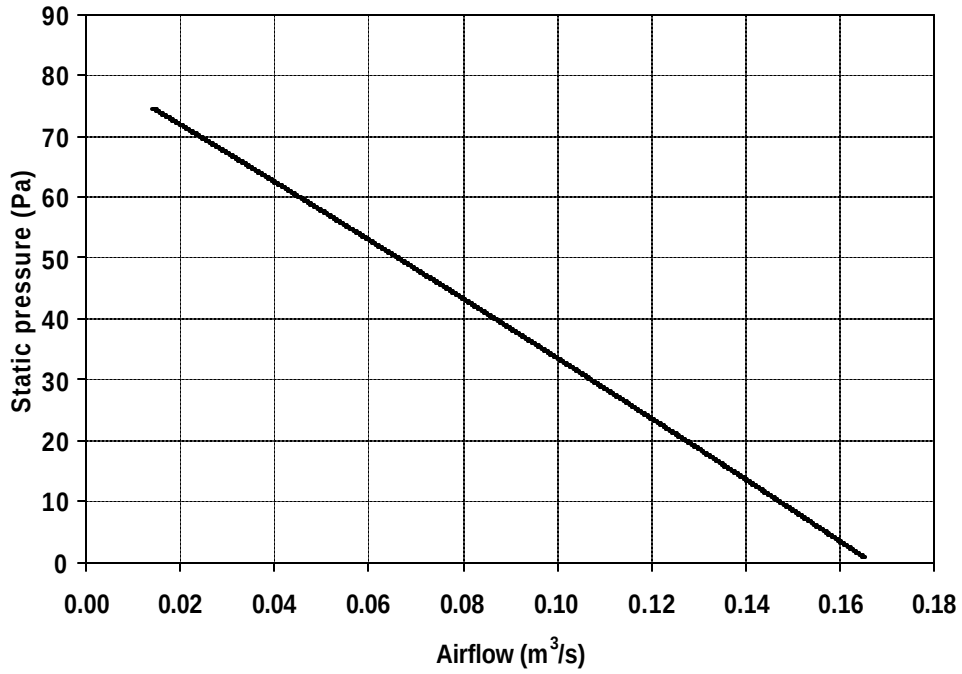

Figure 3.1 Fan Curve

For the display case simulated the air curtain breaks down and defrost is initiated at ~530 cfm, at a sensible capacity of ~2.6 kW corresponding to -3.3 ^{o}C discharge air temperature. To achieve an acceptable defrost interval, the case was designed to deliver (at startup following defrost) 33 % more air flow rate (~707 cfm) corresponding to a sensible capacity of ~2.8 kW, with the same discharge air temperature as seen in Figures 3.2(a)-(d). Defrost was then timed to occur after ~ 4.8 hours of operation to allow air flow to remain always above the breakdown condition during the entire cycle. The simulations were continued past the defrost time, until the algorithm failed after ~8 hours of running when frost had occluded 77 % of the initial free flow area.

The air entrainment fraction increases as air flow rate decreases, causing higher return air temperatures as shown in Figure 3.2(b). The discharge air temperature decreases slightly as a result of two offsetting trends: decreasing air flow; and increasing return air temperature. The reduction in free flow area due to the blockage effect of the frost actually increases the air-side heat transfer coefficient (velocity increases faster due to area constriction than it decreases due to air-side pressure drop).

Prior to defrost initiation, sensible capacity declined because the decreasing air flow rate dominated the increasing return air temperature, as shown in Figure 3.2(c). If defrost was not initiated at 4.8 hours, the simulations suggest that changes in the return air temperature would become dominant, causing the sensible capacity to rise.

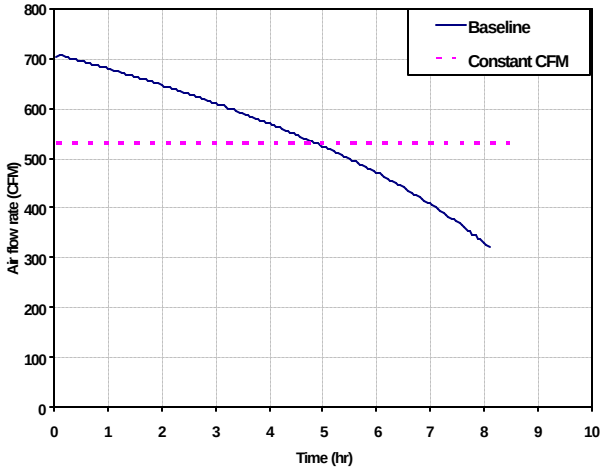

a) Air flow rate

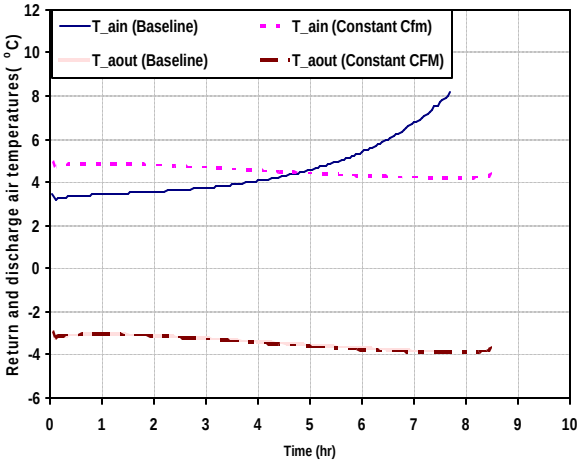

(b) Return and discharge air temperatures

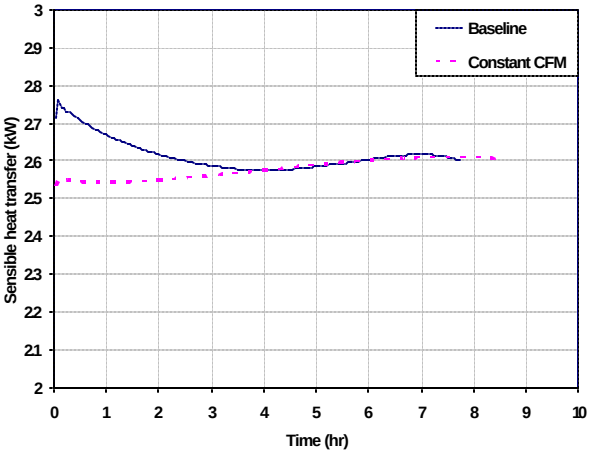

c) Sensible capacity

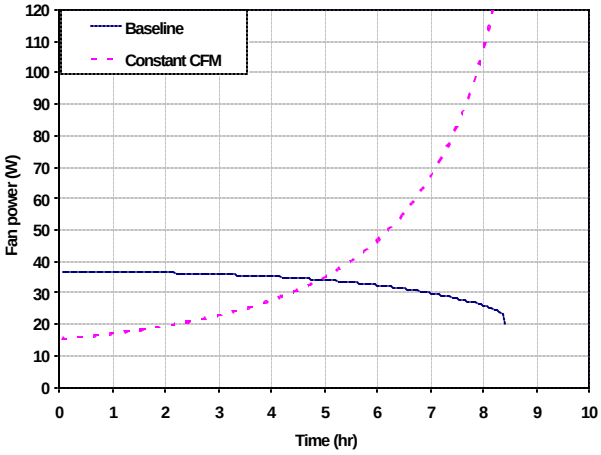

(d) Fan power

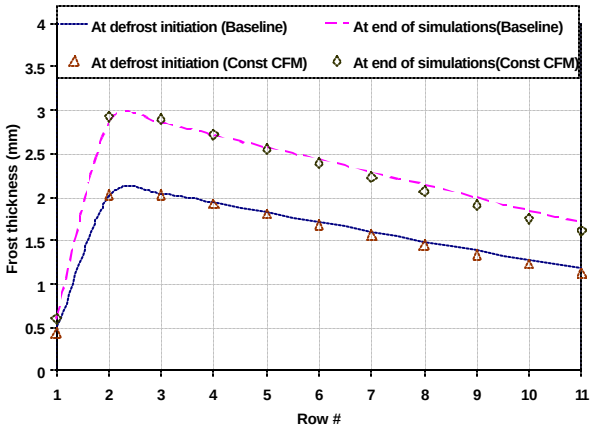

e) Frost thickness distribution

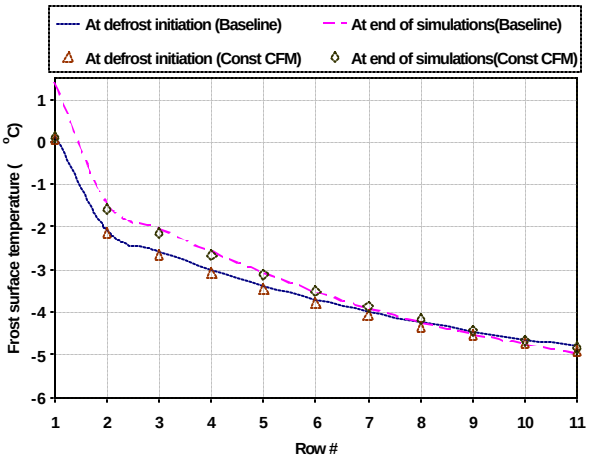

(f) Frost surface temperature distribution

Figure 3.2 Comparison of variable (baseline) and constant air flow operation

3.1.2 Constant air flow

Time between defrosts could theoretically be extended by using a variable-speed fan, and gradually increasing its voltage to maintain a constant 530 cfm as frost blocked the free flow area. The results are designated "constant cfm" in Figures 3.2(a)-(f). Since the "constant air flow" is initially lower, air curtain entrainment is ~23 %, compared to ~19 % in the baseline; presumably this could be improved by redesigning the curtain for constant air flow, but that redesign option was not considered in this example. Figure 3.2(b) shows that the return air temperature was initially higher for constant air flow and declines steadily. Recall that it increased sharply after ~5 hours for baseline operation, as air flow rate dropped below the breakdown level as frost blockage continued to reduce air flow rate and increase entrainment in the standard display case.

For constant air flow operation (with variable-speed fan) a lower refrigerant temperature was selected (-6.3 ^{o}C, compared to -6.2 ^{o}C for the baseline operation) to ensure that the initial discharge air temperature was the same as for baseline operation. This produced a sensible capacity (equal to the breakdown value, 2.6 kW) lower than the baseline design capacity (2.8 kW). Figure 3.2(c) also shows how the sensible capacity for constant air flow operation increased slowly but steadily over time as the air-side heat transfer coefficient increased due to blockage of the free flow area. With sensible capacity increasing and return air temperatures dropping with time, the discharge air temperature dropped over time (identically as the baseline operation) as shown in Figure 3.2(b).

Unexpectedly, for constant air flow operation, the frost thickness and deposition rates were almost the same as baseline operation (Figure 3.2(e)), because the surface temperature distribution was the same for both (Figure 3.2(f)). The simulations revealed that the return air humidity was higher (due to higher store air entrainment) for the constant air flow operation, but this higher absolute humidity gradient between the air and frost surface was offset by the lower air-side heat (mass) transfer coefficient associated with the lower (constant) air flow rate.

As seen in Figure 3.2(d), the fan power requirement for the baseline operation was initially higher and dropped monotonically over time as air flow rate decreased due to frost blockage. To maintain constant air flow operation, with air-side pressure drop increasing over time, the fan power requirement increased from ~15 W (initially) to ~100 W (after 8 hours) to maintain a constant air flow. Averaged over 8 hours, the fan power was 28 % (~7 W) greater than the 4.8 hour average for the baseline (constant speed fan) operation.

3.1.3 Fin Staging

Another strategy explored for decreasing defrosting frequency was fin staging. By varying fin pitch along the air flow direction variations in frost thickness can be accommodated. Several patterns chosen based on manufacturing feasibility (e.g. multiples of 2 as shown in Figure 3.3 and not in fractions) are listed in Table 1 along with the respective refrigerant inlet temperature. The patterns were chosen so that the total air-side pressure drop was the same as for the baseline operation, so the total amount of fin surface area as well as its distribution varied from pattern to pattern. The designation "1-4/5-11" in Table 1 denotes a type of fin staging where rows 1-4 contain half as many fins as rows 5-11. For all simulations, the total number of fins and their distribution was chosen to have the same initial air flow rate (i.e. same overall air-side pressure drop) as the baseline operation. Also the refrigerant inlet temperature was chosen to give the same display case discharge air temperature as in baseline operation. Holding initial air flow rate and case discharge air temperature constant would ensure that the product temperature at the start of each simulation was the same as that for the baseline. The change in COP was estimated using a

performance map for an R404A scroll refrigeration compressor (Copeland ZS45K4E) typically used in supermarket applications.

Figure 3.4(a) compares baseline and various fin staging simulations, in terms of free flow area at each tube row along air flow direction. It was found that the most uniform free flow area distribution was obtained when the transition to twice fin density occurred at 9^{th} tube row. However, not much was gained in terms of the defrost initiation time, (i.e. time at which air flow has decreased by 33%) due to loss of fin surface area. The maximum time gained (~15 minutes) was for fin staging designated "1-4/5-11" in Table 1 and the comparison between the baseline operation and this particular fin staging is shown in Figures 3.4(b) & (c).

By moving the transition tube row in the upwind direction, the refrigerant inlet temperature could be raised and COP improved, mainly due to the net increase in the air-side surface area. For example with "1-4/5-11" type of staging, the refrigerant inlet temperature could be raised from -6.2 ^{o}C (baseline operation) to -5.6 ^{o}C, increasing COP by as much as 1.4 %. The time variation of return and discharge air temperatures, capacity and total frost mass deposition was found to be the same for both baseline and staggered fin operations. Similar trends were observed for all fin staging simulations shown in Table 1.

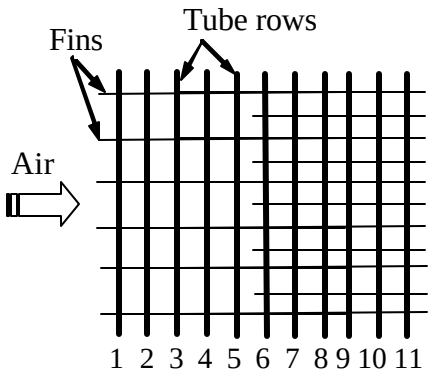

Figure 3.3 Fin staging schematic

Table 3.1 Comparison of evaporating temperature, % change in COP and total air-side surface area for uniform fin pitch (baseline) and fin staging simulations

Designation	Fs (mm)	$T_{r,in}$ (^{o}C)	COP (%)	A_o (%)
Baseline	Row # 1-11 (8.3)	-6.2	0.00	0.0
1-4/5-11	Row # 1-4 (12.97) Row # 5-11 (6.36)	-5.6	+1.42	5.2
1-6/7-11	Row # 1-6 (12.24) Row # 7-11 (6.00)	-5.8	+0.94	-0.3
1-7/8-11	Row # 1-7 (11.94) Row # 8-11 (5.85)	-5.9	+0.71	-3.8
1-8/9-11	Row # 1-8 (11.72) Row # 9-11 (5.74)	-6.2	0.00	-8.0

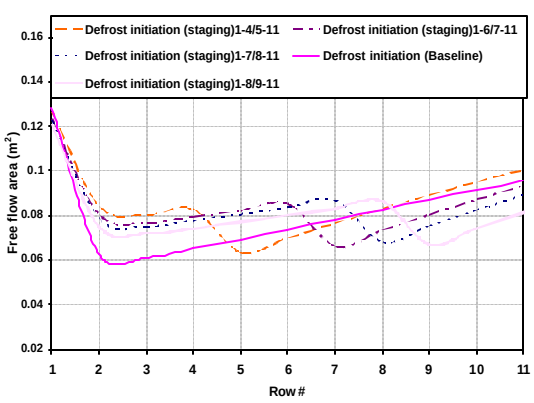

(a) Free flow area across hx

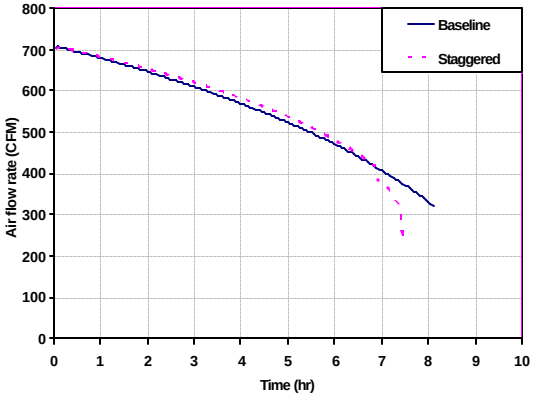

(b) Air flow rate

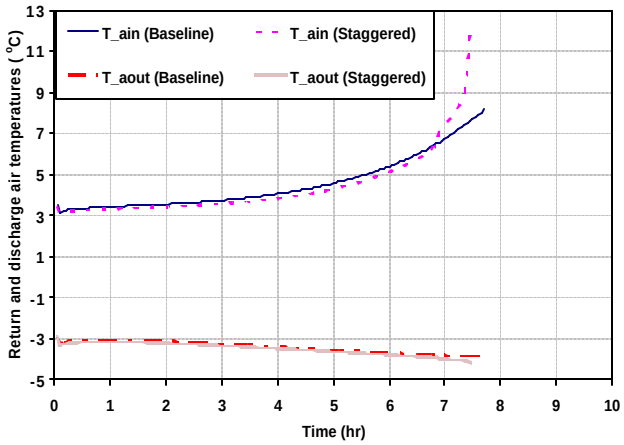

(c) Case return and discharge air temperatures

Figure 3.4 Comparison of uniform fin pitch (baseline) and fin staging simulations

3.2 Conclusion

To understand the mechanisms by which frost degrades evaporator performance a simulation model, originally developed and validated for a secondary refrigerants, was extended to simulate the time- varying operating conditions of supermarket display case with a direct expansion evaporator. Simulations were done to explore two strategies for reducing the defrost frequency: using a variable speed fan to maintain constant air flow rate; and fin staging.

The results shown in Figure 4(a-f) suggest that the defrost interval could be extended from ~4.8 to about 8 hours by using a variable-speed fan to maintain a constant air flow. A net energy savings would result only if the additional energy consumption due to increased fan (28%) and compressor power were offset by the energy savings resulting from less frequent defrosting. In addition, the product temperature may be lower with less frequent defrosts due to reduced number of product temperature excursions associated with each defrost cycle.

A second set of simulations demonstrated how fin staging may provide significant performance enhancements, even when the baseline frost distribution is already quite uniform. In other situations where frost blocks the front rows very early (e.g. when face velocity is lower or inlet humidity is higher), the fin staging can extend defrost intervals even more, while at the same time reducing the cost of fin material required.

Chapter 4: Flat Tube Plain Fin Analysis

4.1 Introduction

This chapter explores a new concept: flat tube/microchannel heat exchangers for commercial applications. For same face velocity and face areas, flat tube is expected have a lower air-side pressure drop in comparison to a round tube due to its streamlined profile and reduced blockage. Thus more free flow area would be available and defrost initiation can be prolonged due to less reduction in the air flow rate. So if a finned flat tube heat exchanger can give the desired sensible capacity then it could be a better alternative to a finned round tube heat exchanger. Moreover, manufacturing of a flat tube heat exchanger with variable fin pitch (different for each tube row) may be simpler than a fin staging in multiples of two as discussed in Chapter 3.

This chapter presents a simple analysis comparing the performance of a flat-tube plain fin heat exchanger with that of a typical round-tube plain-fin medium temperature display case cross-counterflow heat exchanger (Coil V.1: Hill-Phoenix, OHM-8') under dry conditions.

4.2. Single flat-tube plain-fin analysis

4.2.1 Model

A simple flat tube heat exchanger can be viewed as a collection of several single finned flat tubes each having identical fin and tube dimensions. By assembling a number of those individual circuits to match the UA of the baseline coil (coil V.1), the resulting capacity and exit air conditions would also be matched. Comparison was made for a module fitting in the existing core width (~2 m) and height (~0.194 m) of V.1 and based on the performance of a flat tube heat exchanger the depth was allowed to vary. So the package dimensions constraint was the width, height and depth as that of coil V.1. Assuming sensible heat transfer to be ~65 % (determined by the model presented in Chapter 2) of the total for coil V.1, comparison was made by matching the sensible heat transfer of coil V.1 (~2.1 kW).

Each flat tube was analyzed for the same log mean temperature difference (LMTD) as that of coil V.1. While the flat tubes at the leading edge will see higher air temperatures than the ones at the trailing edge, the overall heat exchanger LMTD would be the same if each tube was considered operating at the same LMTD.

The face velocity; air and refrigerant inlet conditions; and fin and tube geometry for the flat-tube plain-fin model are listed in Table 4.1. The geometry and inlet conditions were chosen to meet the specifications of coil V.1. The model uses the LMTD (log mean temperature difference) approach to determine the capacity; Wattelet and Chato (1994) correlation for two-phase refrigerant-side heat transfer; Gnielinsky (1976) correlation for single-phase refrigerant-side heat transfer; Zhang and Kwang (1999) correlation for two-phase refrigerant side pressure drop. As a first approximation, Granryd's (1999) correlation for channel flow (between fins) was used to determine the air-side heat transfer coefficient. Actually the air-side heat transfer coefficient for a finned tube would differ slightly from that for fins (channel) only, but for this analysis the effect of tubes on air-side heat transfer coefficient was neglected and the heat transfer coefficient computed for a channel flow was also applied to the tubes.

Since the flat-tube heat exchanger is made up of small rectangular fins attached to each tube, it will exhibit better air-side performance, because of the increased air-side heat transfer coefficient due to restarting of the thermal boundary layer as air passes over the flat tube heat exchanger (normal to a series of several finned flat tubes). Recall

that coil V.1 had continuous fins resulting in much lower air-side heat transfer coefficient. A more detailed analysis is presented below.

Different tube widths and tube heights were simulated to obtain tube lengths that would produce a 5 ^{o}C superheat (same as coil V.1) and refrigerant-side pressure drop corresponding to a saturation temperature drop of 0.5 ^{o}C. Thus the two opposing effects of increasing tube width: decrease of air-side heat transfer coefficient; and increase in surface area could be exploited to obtain a geometry that lies within the package dimensions of coil V.1. The optimal fin height was calculated assuming arbitrarily a 90 % dry fin efficiency, and fin depth was assumed to be the sum of tube outer width (tube width plus tube wall thickness on both sides) plus half the fin height (half of which is on the upwind side of the tube, the other half on downwind) as shown in Figure 4.1. On the refrigerant-side, the increase in the cross-sectional area allows an increased tube length (mass flux decreases). For this family of geometries, any increase in the tube height or width is accompanied by an increase in fin area per unit length. Thus an increase in tube height or width results in an increase in the heat transfer due to two reasons: longer tube lengths (lower mass flux of refrigerant); and more air-side area (increased fin area) per unit tube length.

Table 4.1 Specifications of Hill-Phoenix (V.1) coil and flat tube geometry

	V_{face} (m/s)	$T_{a,in}$ (^{o}C)	$T_{r,in}$ (^{o}C)	LMTD (^{o}C)	Fs (mm)	f_{th} (mm)	Dc (mm)	Core height (m)	Core depth (m)	Core width (m)	super-heat (^{o}C)	dT_{sat} (^{o}C)	x_{in}
Coil V.1	0.57	2.8	-8.3	8.3	12.7	0.2	12.7	0.194	0.305	1	5	-	0.4
Flat tube	0.57	0.05	-8.3	8.3	12.7	0.2	-	-	-	1	5	0.5	0.4

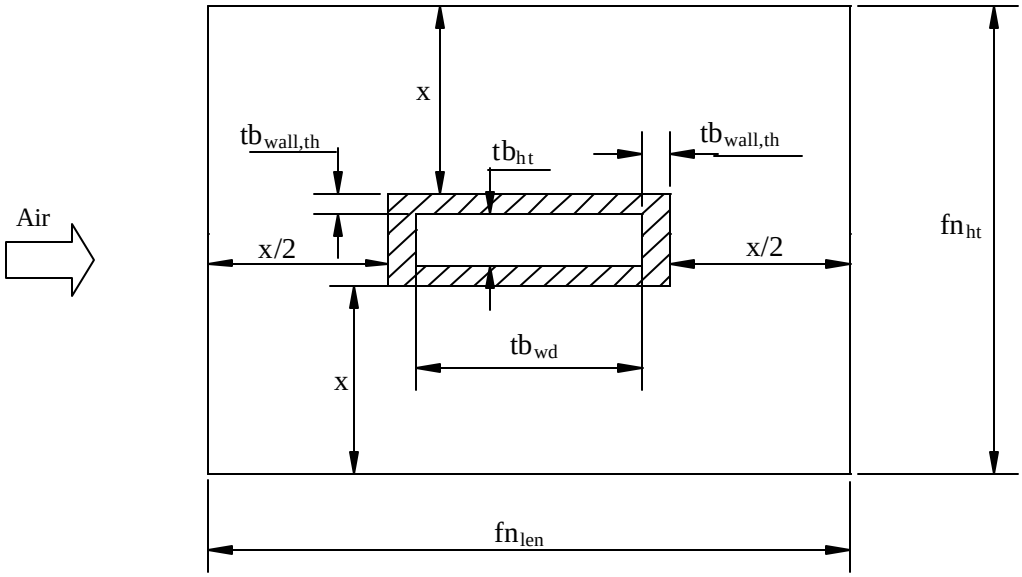

Figure 4.1 Flat-tube plain-fin schematic

4.2.2 Results

Three tube heights were considered for simulations: 1.5 mm; 2 mm; and 2.5 mm. The simulation results are presented in Figure 4.1-4.5. Figure 4.1 shows the variation of air-side heat transfer coefficient with tube width for different tube heights. Clearly for a given tube height, the air-side heat transfer coefficient would decrease as the fin length (in the air flow direction) increases with increasing tube width. As expected the tube height has an insignificant effect on the air-side heat transfer coefficient. However, as shown in Figure 4.2, greater tube height results in higher heat transfer due to increased fin height and hence more surface area. While air-side heat transfer coefficient is insensitive to tube height, the capacity increases with increasing tube width due to the addition of surface area (increasing fin length). Thus in terms of heat transfer alone, tube height of 2.5 mm with tube width greater than 10 mm proves to be better than the other two tube heights considered.

Although the 2.5 mm tube height has relatively more heat transfer than the other two, the simulated single-tube length requirement (for 0.5 ^{o}C saturation temperature drop and 5 ^{o}C superheat) is also longest, as shown in Figure 4.3. As expected the tube length increases with tube width and for a given tube width it increases with tube height. As tube cross-sectional area increases, the refrigerant mass flux decreases, and a longer tube can be tolerated. While the difference in the tube length for various tube heights is initially lower and increases with tube width, the fin height increases almost linearly with tube height for the entire tube width range considered as shown in Figure 4.4. The tube width impacts the fin height because a change in the air-side heat transfer coefficient leads to a change in the fin parameter (used in fin efficiency). The effect of tube height on fin length was found to be insignificant (Figure 4.5) while it increases with increasing tube width due to increased fin height.

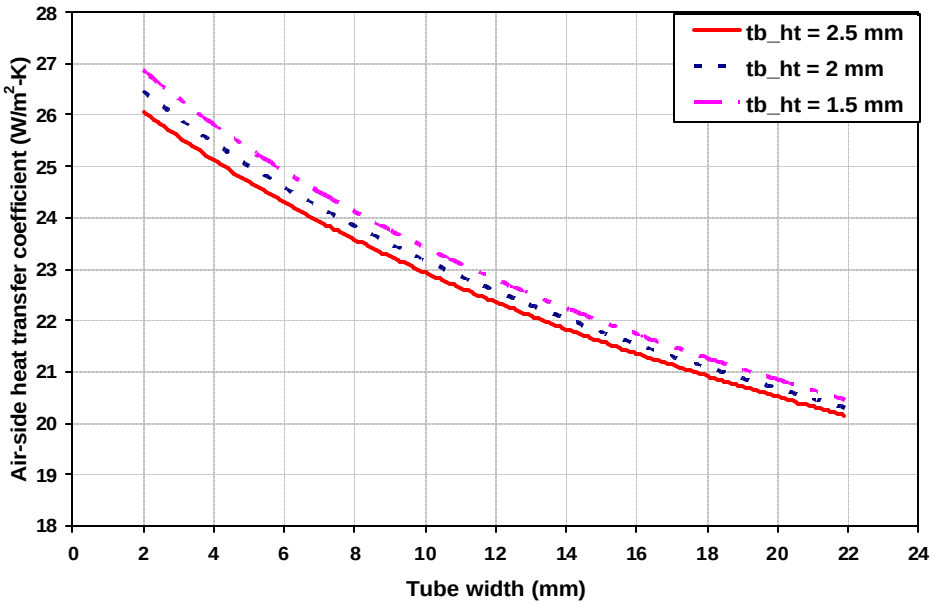

Figure 4.2 Variation of air-side heat transfer coefficient with tube width and tube height

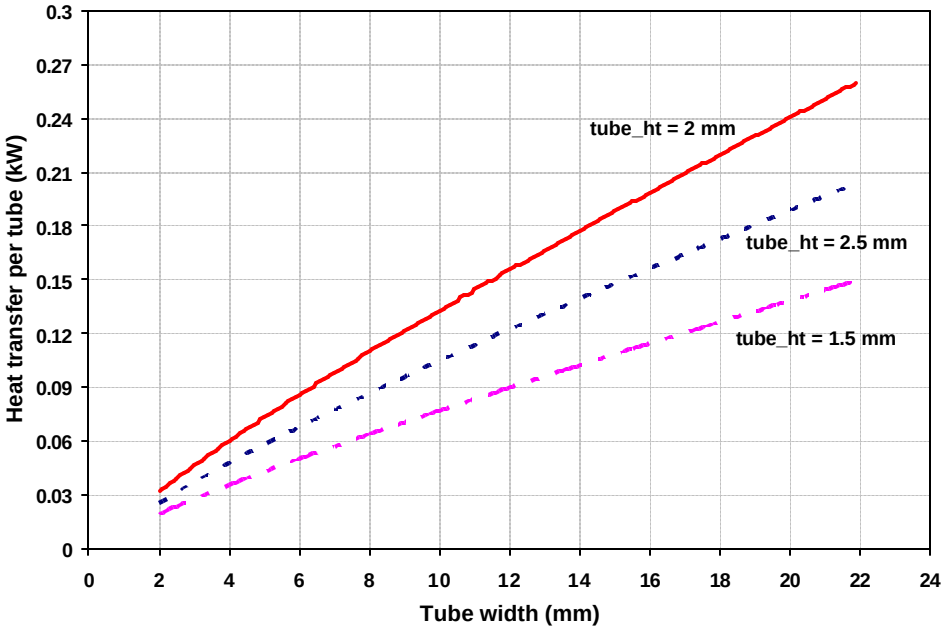

Figure 4.3 Variation of heat transfer with tube width and tube height

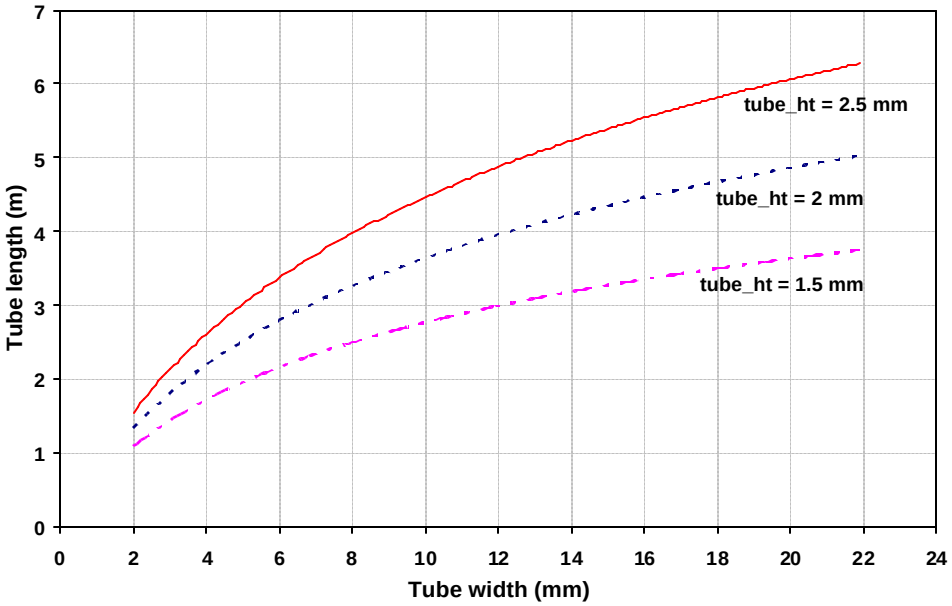

Figure 4.4 Variation of tube length with tube width and tube height

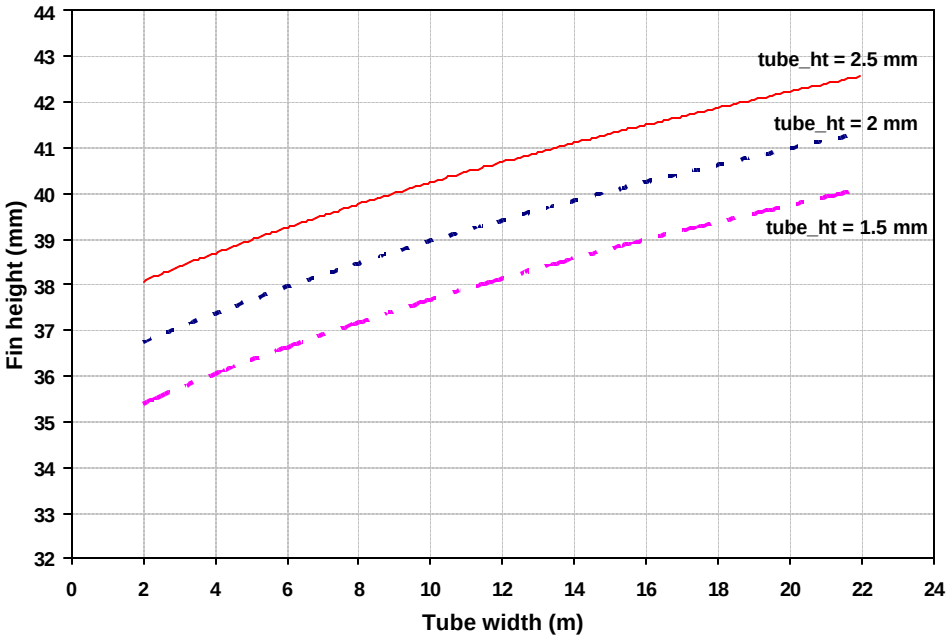

Figure 4.5 Variation of fin height with tube width and tube height

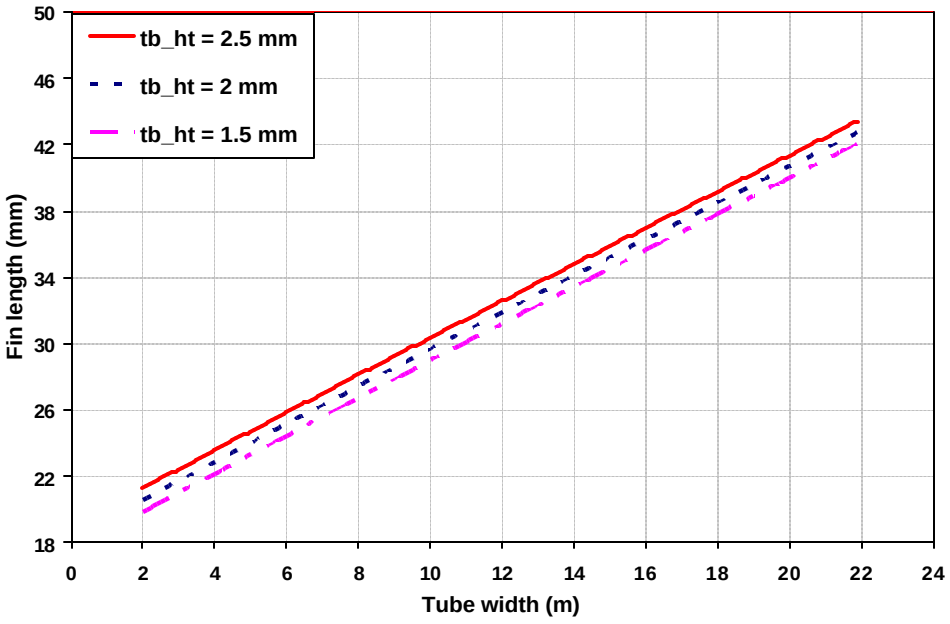

Figure 4.6 Variation of fin length with tube width and tube height

Tables 4.2, 4.3, and 4.4 show on a per circuit basis : the package volume; air-side area; and air flow rate for single tubes of several widths, for 2.5 mm, 2 mm, and 1.5 mm tube height respectively. For each tube height, the tube widths considered are those that fit the package dimensions of coil V.1 as per the conditions given in section 4.3 below. As shown the number of fins and hence air-side (fin and tube surface) area, increases with tube height due to an increase in the tube length (Figure 4.3). However the per unit values for: package volume; air-side area;

and air flow rate are almost the same for different tube heights considered, since with an increase in the number of fins, the heat transfer increases (Figure 4.2). In comparison to coil V.1, all single flat-tube results shown in Tables 4.2, 4.3, 4.4 have lower air-side area per unit capacity and hence lower package volume per unit capacity. This is primarily due to higher air-side heat transfer coefficient for flat tubes (shorter fin length in the air flow direction).

Table 4.2 Single tube results for 2.5 mm tube height

tb_{wd} (mm)	$Q_{circuit}$ (W)	h_a (W/m^{2}K)	N_{fin}	A_{fin} (m^2)	A_{tube} (m^2)	$Vol/Q_{circuit}$ (m^3/W)	$A_{air}/Q_{circuit}$ (m^2/W)	$\dot{V}_{air}/Q_{circuit}$ (m^3/s/W)
2.1	32.1	26.1	123	0.19	0.03	3.9E-05	7.0E-03	1.1E-03
2.5	39.5	25.8	147	0.24	0.04	3.9E-05	7.0E-03	1.1E-03
3.9	59	25.2	203	0.35	0.06	4.0E-05	7.0E-03	1.0E-03
6.2	88.3	24.2	272	0.53	0.10	4.0E-05	7.1E-03	9.2E-04
10.6	140	22.8	363	0.85	0.17	4.1E-05	7.3E-03	7.9E-04
14	177.3	21.8	413	1.10	0.23	4.2E-05	7.5E-03	7.3E-04
17.1	210.3	21.1	449	1.33	0.29	4.3E-05	7.7E-03	6.8E-04
20	240.4	20.5	478	1.55	0.34	4.4E-05	7.9E-03	6.4E-04
21.5	255.7	20.2	491	1.66	0.37	4.5E-05	7.9E-03	6.2E-04
Coil V.1	2100	15	162	16.52	3.88	5.5E-05	9.7E-03	1.1E-04

Table 4.3 Single tube results for 2 mm tube height

tb_{wd} (mm)	$Q_{circuit}$ (W)	h_a (W/m^{2}K)	N_{fin}	A_{fin} (m^2)	A_{tube} (m^2)	$Vol/Q_{circuit}$ (m^3/W)	$A_{air}/Q_{circuit}$ (m^2/W)	$\dot{V}_{air}/Q_{circuit}$ (m^3/s/W)
2.3	29.5	26.3	118	0.18	0.03	3.9E-05	6.9E-03	1.1E-03
2.8	35.1	26.0	136	0.21	0.03	3.9E-05	6.9E-03	1.1E-03
3.2	39.5	25.8	150	0.24	0.04	3.9E-05	6.9E-03	1.1E-03
5.1	59.3	25.0	200	0.35	0.06	3.9E-05	7.0E-03	9.7E-04
8.4	90.6	23.7	264	0.54	0.10	4.0E-05	7.1E-03	8.5E-04
15.3	150.4	21.7	346	0.93	0.19	4.2E-05	7.5E-03	7.0E-04
18.6	177.6	21.0	373	1.12	0.24	4.3E-05	7.6E-03	6.5E-04
20.1	189.7	20.7	385	1.21	0.26	4.3E-05	7.8E-03	6.3E-04
Coil V.1	2100	15	162	16.52	3.88	5.5E-05	9.7E-03	1.1E-04

Table 4.4 Single tube results for 1.5 mm tube height

tb_{wd} (mm)	$Q_{circuit}$ (W)	ha (W/m^2K)	N_{fin}	A_{fin} (m^2)	A_{tube} (m^2)	$Vol/Q_{circuit}$ (m^3/W)	$A_{air}/Q_{circuit}$ (m^2/W)	$\dot{V}_{air}/Q_{circuit}$ ($m^3/s/W$)
2.8	26.4	26.4	109	0.07	0.11	3.9E-05	6.9E-03	1.1E-03
3.3	39.4	26.2	121	0.08	0.12	3.0E-05	5.3E-03	8.3E-04
4.5	39.6	25.6	146	0.11	0.15	3.8E-05	6.7E-03	1.0E-03
8.5	67.4	23.9	203	0.20	0.23	3.9E-05	6.5E-03	8.5E-04
9.8	75.9	23.5	217	0.23	0.26	3.9E-05	6.4E-03	8.1E-04
16.4	117.0	21.6	267	0.39	0.36	4.1E-05	6.4E-03	6.8E-04
20	138.4	20.8	287	0.49	0.41	4.2E-05	6.5E-03	6.2E-04
21.9	149.6	20.5	296	0.54	0.44	4.2E-05	6.5E-03	6.0E-04
Coil V.1	2100	15	162	16.52	3.88	5.5E-05	9.7E-03	1.1E-04

4.3 Flat tube heat exchanger configurations

Tables 4.5, 4.6, and 4.7 summarize the results of flat tube heat exchanger analysis (tube heights of 2.5 mm, 2 mm, and 1.5 mm respectively) and lists: total number of circuits, and depth of the heat exchanger with total height and total width and total sensible capacity being the same as coil V.1.

As quantified in the tables, the flat tube heat exchanger depth was nearly the same for all tube heights considered (negligible change in air-side heat transfer coefficient with tube height) and increased with increasing tube width (increasing fin and circuit length). As shown in Tables 4.5-4.7, an increase in the tube width from almost square cross-section to higher tube widths the total number of circuits gets reduced by ~6 times. The total heat exchanger depth could be reduced by 22 % (with as few as 10 circuits) compared to baseline and ~28 % if willing to go to ~54 circuits and basically round tubes with an hydraulic diameter of 2.5 mm The design of flat tube heat exchanger would be selected after comparing the cost of individual brazing (possible with lowest number of circuits) to that of combined brazing (more than ~12 number of circuits). This difference in brazing costs (manual vs. furnace) would be compared to the value of the reduction in the heat exchanger depth saved by using flat tubes.

Table 4.5 Possible flat tube heat exchanger configurations for 2.5 mm tube height

tb_{wd} (mm)	fn_{ht} (mm)	Len_{tb}/Cir (m)	Total no. of circuits	Total depth (m)
2.5	38.2	1.86	54	0.216
3.9	38.7	2.57	36	0.216
6.2	39.3	3.44	24	0.219
10.6	40.4	4.60	16	0.238
17.1	41.7	5.70	10	0.234

Table 4.6 Possible flat tube heat exchanger configurations for 2.0 mm tube height

tb_{wd} (mm)	f_{ht} (mm)	Len_{tb}/Cir (m)	Total no. of circuits	Total depth (m)
2.3	36.8	1.50	72	0.214
3.2	37.1	1.89	54	0.215
5.1	37.7	2.55	36	0.215
8.4	38.6	3.35	24	0.223
15.3	40.1	4.39	14	0.226
18.6	40.7	4.74	12	0.234

Table 4.7 Possible flat tube heat exchanger configurations for 1.5 mm tube height

tb_{wdth} (mm)	fn_{ht} (mm)	Len_{tb}/Cir (m)	Total no. of circuits	Total depth (m)
2.8	35.7	1.38	80	0.211
3.3	35.8	1.54	70	0.212
4.5	36.2	1.85	54	0.212
8.5	37.3	2.58	32	0.216
16.4	39.1	3.39	18	0.222
20	39.7	3.64	16	0.239

4.4 Conclusion

From the above preliminary single flat tube analysis we can conclude that a flat- tube-plain-fin heat exchanger with discontinuous fins has better heat transfer performance than an existing plain-fin-round-tube heat exchanger with continuous fins, and also anticipated to have lower air-side pressure drop (not included in the analysis) due to reduced overall depth and less blockage per tube row due to the flat tubes. Perhaps the freedom to choose arbitrarily the fin spacing for each tube bank could allow even better performance by lessening deterioration of free flow area as frost accumulates. This preliminary analysis could be incorporated in the form of a frosting model (similar to one presented in Chapter 2) with a more accurate air-side heat transfer coefficient and addition of air-side pressure drop and latent heat transfer. Thereby the plain-fin flat-tube heat exchanger frosting model could be used to develop design guidelines to reduce overall energy consumption or maximize COP.

Chapter 5: Conclusions

1. A design tool for simulating the performance of a display case heat exchanger performance under frosting conditions was developed. The simulation model is an extension of an experimentally-validated model for secondary (single phase) refrigerant and constant operating conditions. It relies on underlying physical heat and mass transfer and well established correlations for: air-and-refrigerant-side heat transfer and pressure drop, frost density; and frost thermal conductivity and predicts spatial and temporal distribution of frost deposition and its effect on heat exchanger performance. The model captures the performance degradation due to frost buildup in terms of increase in the air-side pressure drop and decrease in the heat transfer. Then fan curve characteristics are used to incorporate reduction in the air flow rate; a curve fit of experimental data is used to simulate the ambient air infiltration into the air curtain as a function of air flow rate; and various loads on the display case such as lighting, infiltration and fan power are accounted for in the analysis.

2. Based on a few simple defrosting assumptions the equations for determining the defrost time and compressor and fan energy requirements are presented in a separate model. Thus the display case heat exchanger could be analyzed for frosting and defrosting, providing a tool to design display case heat exchangers based on optimal overall energy consumption.

3. Two design strategies for reducing defrost frequency and overall energy consumption of open supermarket display cases were evaluated relative to the baseline (varying air flow as a consequence of fan characteristics) operation: constant air flow operation; and fin staging. Results suggest that the defrost interval could be extended from 4.8 hours to 8 hours by employing a variable-speed fan to maintain constant air flow. The energy efficiency penalty was quantified in terms of increased fan and compressor energy requirements for comparison with energy savings resulting from less frequent defrosts. Fin staging is also shown to result in significant performance improvements, especially at low face velocities and high inlet humidities where most of the frosting occurs near the front of the heat exchanger.

4. A preliminary study of single flat-tube plain-fin analysis was conducted under dry conditions. Based on that analysis, a few designs of a flat-tube-plain-fin heat exchanger with discontinuous fins are presented. All the designs presented exhibit better heat transfer than an existing display case round-tube-plain-fin heat exchanger, mainly due to the interruption of fins after each tube row. Apart from better heat transfer, the designs presented are also expected to have lower air-side pressure drop due to lower depth in air flow direction and the use of flat tubes instead of round tubes. This preliminary study could be extended to simulate frosting of a flat-tube-plain-fin heat exchanger with arbitrary fin spacing for each tube row, optimizing the variation of free flow area from the leading to the trailing edge. These preliminary results suggest that this may be an effective strategy for prolonging the time between defrosts.

Appendix A: Heat Transfer and Pressure Drop Correlations

A.1 Air-side heat transfer coefficient correlations

A.1.1 Wang et al. (2000)

$$h_{a,Wang} = j_{Wang} \cdot G_{a,\max} \cdot C_{p,a} \cdot \Pr^{-2/3} \tag{A.1}$$

$$j_{Wang,N\geq 2} = 0.086 \,\mathrm{Re}_{D_c}^{P3} \, N^{P4} \left(\frac{F_p}{D_c}\right)^{P5} \left(\frac{F_p}{D_h}\right)^{P6} \left(\frac{F_p}{P_t}\right)^{-0.93} \tag{A.2}$$

$$P3 = -0.361 - \frac{0.042N}{\log_e(\mathrm{Re}_{Dc})} + 0.158 Log_e\left(N\left(\frac{F_p}{D_c}\right)^{0.41}\right) \tag{A.3}$$

$$P4 = -1.224 - \frac{0.076\left(\frac{P_l}{D_h}\right)^{1.42}}{\log_e(\mathrm{Re}_{Dc})} \tag{A.4}$$

$$P5 = -0.083 + \frac{0.058N}{\log_e(\mathrm{Re}_{Dc})} \tag{A.5}$$

$$P6 = -5.735 + 1.21 Log_e\left(\frac{\mathrm{Re}_{Dc}}{N}\right) \tag{A.6}$$

$$D_h = \frac{4A_{free}L}{A_o} \tag{A.7}$$

A.1.2 Kim et al. (1999)

$$h_{a,Kim} = j_{Kim} \cdot G_{a,\max} \cdot C_{p,a} \cdot \Pr^{-2/3} \tag{A.8}$$

$$j_{N=3} = 0.163 \,\mathrm{Re}_D^{-0.369} \left(\frac{P_t}{P_l}\right)^{0.106} \left(\frac{F_s}{D}\right)^{0.0138} \left(\frac{P_t}{D}\right)^{0.13} \tag{A.9}$$

$$\frac{j_{N=1,2}}{j_{N=3}} = 1.043 \cdot \left[\mathrm{Re}_D^{-0.14} \left(\frac{P_t}{P_l}\right)^{-0.564} \left(\frac{F_s}{D}\right)^{-0.123} \left(\frac{P_t}{D}\right)^{1.17}\right]^{(3-N)} \tag{A.10}$$

A.1.3 Granryd et al. (1999)

$$h_a = K_z \cdot \left(h_{a,cyl} \cdot \frac{A_{a,tube}}{A_{a,total}} + C_h \cdot h_{a,sl} \cdot \left(1 - \frac{A_{a,tube}}{A_{a,total}}\right)\right) \tag{A.11}$$

Table A.1 The factor Kz (When z = 1, Kz = 1)

Re =		**= 1000**	**1500**	**2000**	**3000**	**4000**	**= 5000**
K_z for inline tube arrangement;							
z_r = 1;	z = 2	0.89	0.89	0.90	0.95	1.00	1.05
	3	0.86	0.86	0.87	0.94	1.01	1.06
	(5)	0.83	0.83	0.84	0.93	1.01	1.08
z_r = 2;	z = 2	0.89	0.90	0.94	1.01	1.05	1.05
	3	0.86	0.87	0.92	1.01	1.06	1.06
z_r = 3;	z = 2	0.89	0.95	1.01	1.05	1.05	1.05
	3	0.86	0.94	1.01	1.06	1.06	1.06
K_z for staggered tube arrangement;							
z_r = 1;	z = 2	0.93	0.94	0.97	1.01	1.05	1.05
	3	0.90	0.91	0.95	1.01	1.06	1.06
	(5)	0.88	0.89	0.93	1.01	1.08	1.08
z_r = 2;	z = 2	0.93	0.98	1.02	1.05	1.05	1.05
	3	0.90	0.97	1.02	1.06	1.06	1.06

$$h_{a,cyl} = \frac{Nu_{cyl} k_a}{D_c} \qquad \text{(A.12)}$$

$$Nu_{cyl} = C.\mathrm{Re}_{Dc}^{\ n}.\mathrm{Pr}^{0.33} \qquad \text{(A.13)}$$

The constants C and n are given in Table A.2 below:

Table A.2 Constants C and n for heat transfer in tube bundles

S_l/Dc	S_l/Dc							
	1.25		1.5		2.0		3	
	C	n	C	n	C	n	C	n
In line								
1.3	0.386	0.592	0.305	0.608	0.111	0.704	0.070	0.752
1.5	0.407	0.586	0.278	0.620	0.112	0.702	0.075	0.744
2.0	0.464	0.570	0.332	0.602	0.254	0.632	0.220	0.648
3.0	0.322	0.601	0.396	0.584	0.415	0.581	0.317	0.608
Staggered								
0.6	-	-	-	-	-	-	0.236	0.636
0.9	-	-	-	-	0.495	0.571	0.445	0.581
1.0	-	-	0.552	0.558	-	-	-	-
1.125	-	-	-	-	0.531	0.565	0.575	0.560
1.25	0.575	0.556	0.561	0.554	0.576	0.556	0.579	0.562
1.5	0.501	0.568	0.511	0.562	0.502	0.568	0.542	0.568
2.0	0.448	0.572	0.462	0.568	0.535	0.556	0.498	0.570
3.0	0.344	0.592	0.395	0.580	0.488	0.562	0.467	0.574

$$h_{a,sl} = \frac{Nu_{sl} k_a}{D_h} \quad \text{(A.14)}$$

$$\approx 500 < \mathrm{Re}_{Dh} < 2500 \qquad Nu_{sl} = 2.09.\left(\mathrm{Re}_{Dh}.D_h / L\right)^{0.35} \quad \text{(A.15)}$$

$$2500 < \mathrm{Re}_{Dh} < 7000 \qquad Nu_{sl} = 0.407.\mathrm{Re}_{Dh}^{0.55}.\left(D_h / L\right)^{0.3} \quad \text{(A.16)}$$

$$7000 < \mathrm{Re}_{Dh} < 20000 \qquad Nu_{sl} = 0.3058.\mathrm{Re}_{Dh}^{0.8}.\left(D_h / L\right)^{0.2} \quad \text{(A.17)}$$

$$D_h = \frac{2 \cdot Fs \cdot f_{ht}}{\left(Fs + f_{ht}\right)} \quad \text{(A.18)}$$

$$C_h = 1.05 + K_{\mathrm{Re}}\left(K_A K_{zr} - 1.05\right) \quad \text{(A.19)}$$

The factors K_{Re}, K_A and K_{zr} are given in Table A.3, A.4, and A.5 respectively.

Table A.3 The factor K_{Re}

In-line tube arrangement	
Re<1000	$K_{Re} = 0$
1000 < Re < 6000	$K_{Re} = (Re/1000)^{0.39} - 1$
6000 < Re	$K_{Re} = 1$
Staggered tube arrangement	
Re < 500	$K_{Re} = 0$
500 < Re < 5000	$K_{Re} = (Re/500)^{0.3} - 1$
5000 < Re	$K_{Re} = 1$

$$K_{z_r} = 0.89 + 0.6.\left(1 - \frac{1}{z_r}\right) \quad \text{(A.20)}$$

A.2 Air side pressure drop correlations

A.2.1 Wang et al. (2000)

$$f = 0.0267 \cdot \mathrm{Re}_{Dc}^{F1} \cdot \left(\frac{P_t}{P_l}\right)^{F2} \cdot \left(\frac{F_p}{D_c}\right)^{F3} \quad \text{(A.21)}$$

$$F1 = -0.764 + 0.739\frac{P_t}{P_l} + 0.177\frac{F_p}{D_c} - \frac{0.00758}{N} \quad \text{(A.22)}$$

$$F2 = -15.689 + \frac{64.021}{Log_e(\mathrm{Re}_{Dc})} \quad \text{(A.23)}$$

$$F3 = 1.696 - \frac{15.695}{\log_e(\mathrm{Re}_{Dc})} \quad \text{(A.24)}$$

A.2.2 Kim et al. (1999)

$$f = f_f \cdot \frac{A_{fin}}{A_o} + f_t \cdot (1 - \frac{A_{fin}}{A_o}) \cdot (1 - \frac{F_{th}}{F_p}) \quad \text{(A.25)}$$

Where

$$f_t = \frac{4}{p} \cdot (0.25 + \frac{0.118}{\left[\frac{P_t}{D} - 1\right]^{1.08}} \mathrm{Re}_D^{-0.16}) \cdot (\frac{P_t}{D} - 1) \quad \text{(A.26)}$$

$$f_f = 1.455 \cdot \mathrm{Re}_D^{-0.656} \cdot \left(\frac{P_t}{P_l}\right)^{-0.347} \cdot \left(\frac{F_s}{D}\right)^{-0.134} \cdot \left(\frac{P_t}{D}\right)^{1.23} \quad \text{(A.27)}$$

A.2.3 Granryd et al. (1999)

$$dP_a = z.P_z.\left(\frac{r.V_{sl}^{\ 2}}{2}\right)\left(V_{1,2} + z_r.V_r + \frac{C_f \cdot f_{sl}.L}{2.Fs}\right) \quad \text{(A.28)}$$

The factor P_z is given in Table A.5 below:

Table A.5 The factor P_z (when z = 1, P_z = 1)

Re =		<1000	2000	3000	5000	> 8000
				P_z for inline tube arrangement;		
z_r = 1;	z = 2	0.78	0.81	0.85	0.91	0.91
	3	0.72	0.76	0.81	0.89	0.89
	(5)	0.67	0.71	0.77	0.86	0.86
z_r = 2;3	z = 2	0.85	0.86	0.89	0.91	0.91
	3	0.81	0.83	0.85	0.89	0.89
				P_z for staggered tube arrangement;		
z_r = 1;2	z = 2	0.88	0.89	0.91	0.92	0.93
	3	0.85	0.86	0.88	0.90	0.91
	(5)	0.82	0.83	0.85	0.87	0.89

$$V_{1,2} = \frac{f_{th}}{\left(f_{th} + F_p\right)} \quad \text{(A.29)}$$

$$V_r = V_{10} \cdot \left[\frac{S_t}{S_t - D_c}\right]^2 \quad \text{(A.30)}$$

where t_{10} is given by Figure A.1.

$$500 < \mathrm{Re}_{Dh} < 2000 \qquad f_{sl} = 22.5.\left(\frac{L}{D_h}\right)^{-0.3}.\mathrm{Re}_{Dh}^{-0.65} \quad \text{(A.31)}$$

$$2000 < \mathrm{Re}_{Dh} < 7000 \qquad f_{sl} = 3.35.\left(\frac{L}{D_h}\right)^{-0.3}.\mathrm{Re}_{Dh}^{-0.4} \qquad \text{(A.32)}$$

$$7000 < \mathrm{Re}_{Dh} < 20000 \qquad f_{sl} = 0.577.\left(\frac{L}{D_h}\right)^{-0.3}.\mathrm{Re}_{Dh}^{-0.2} \qquad \text{(A.33)}$$

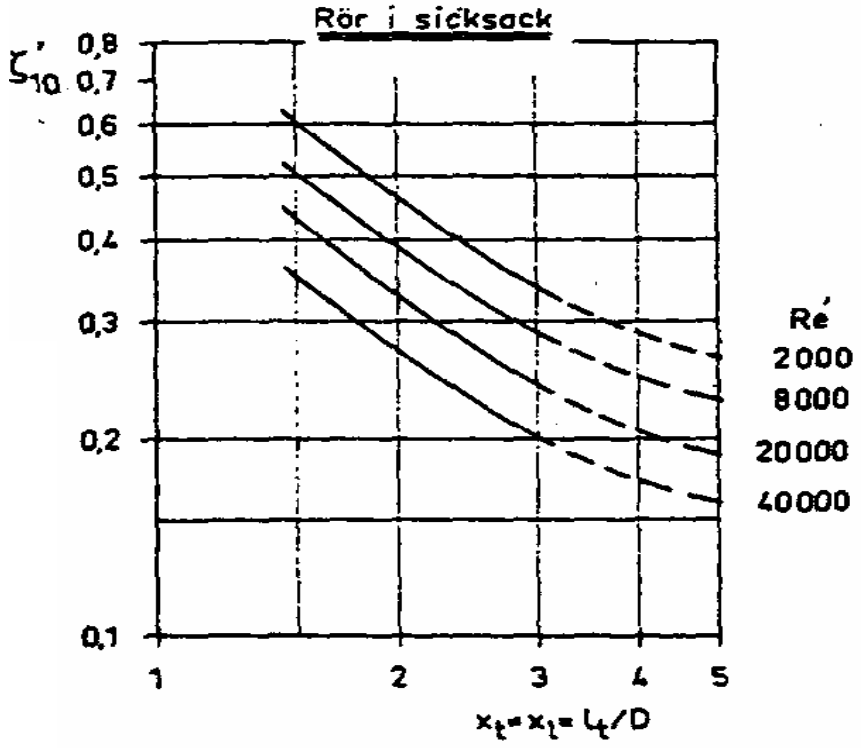

Figure A.1 The parameter t_{10}.

$$Cf = f\left[\left(\frac{\mathrm{Re}}{10000}\right)^{n} \cdot 8.4 \cdot \frac{D_c}{S_t} + 0.05\left|\frac{S_t}{D_c} - 3\right|\right] \qquad \text{(if } 700 < \mathrm{ReD_h} < 10000\text{)} \qquad \text{(A.34)}$$

where

$\phi = 1$ for in-line tube arrangement, and

$\phi = 1.05$ for staggered tube arrangement.

Note: For $z_r = 1$, $\phi = 1$ also in staggered arrangement.

$n = 0.05$ for $z_r = 1$

$= 0.17$ for $z_r = 2$

$= 0.25$ for $z_r = 3$

A comparison of the range of each correlation with the considered heat exchanger geometries is given in Appendix B

A.3 Refrigerant-side heat transfer correlations

A.3.1 Single-phase heat transfer

The Gnielinski correlation for fully developed (hydro-dynamically and thermally) turbulent flow in a smooth circular tube was used for single phase flow The correlation is expressed in Equation B.13.

$$Nu = \frac{(f/8)(\mathrm{Re}_{di} - 1000)\mathrm{Pr}_{ref}}{1 + 12.7(f/8)^{1/2}\left(\mathrm{Pr}_{ref}^{2/3} - 1\right)} \tag{A.35}$$

Where f friction factor

Re_{di} Reynolds number based on inner tube diameter

Pr_{ref} Refrigerant Prandtl number

This correlation is valid for $0.5 < \mathrm{Pr} < 10^6$, $2300 < \mathrm{Re}_{di} < 5\text{x}10^6$.

The friction factor comes from the following equations:

$$Term = 2.457 \ \ln \frac{1}{(7/\mathrm{Re}_{di})^{0.9} + 0.27 \ \ \mathrm{Re}\, lrough} \tag{A.36}$$

$$A = Term^{16} \tag{A.37}$$

$$B = (37530/\mathrm{Re}_{di})^{16} \tag{A.38}$$

$$Term_2 = \frac{1}{(A+B)^{3/2}} \tag{A.39}$$

$$Term_1 = \frac{8}{\mathrm{Re}_{di}} \tag{A.40}$$

$$f = 8 \ (Term_1^{12} + Term_2)^{1/12} \tag{A.41}$$

Relrough is the relative roughness of the tube surface and can be expressed in Eqn. A.42 (ASHARE Fundamentals, 1987):

$$\mathrm{Re}\, lrough = \frac{1.5 * 10^{-6}}{di} \tag{A.42}$$

Generally speaking, the thermal entry length x_{fd} in turbulent flow will affect the heat transfer coefficient. Incropera and DeWitt (1996) defined x_{fd} as: $\frac{x_{fd}}{di} = 10$. Kays and Crawford (1993) analyzed the effect of thermal-entry-length on the heat transfer coefficient for turbulent flow in a circular tube. They found that for small Prandtl numbers, this effect is very pronounced and increases with Reynolds number. However, at Prandtl number above 1, the thermal-entry-length effect becomes less and less important.

Their results show that at Pr=10 and Re=100,000, when $x/d_i=0$, $Nu_x/Nu_{fd}=1.05$; when $x/d_i=10$, $Nu_x/Nu_{fd}=1.02$; when $x/d_i=20$, $Nu_x/Nu_{fd}=1.01$; and at $x/d_i > 30$, the local Nusselt number is almost the same as the fully developed flow Nusselt number, which means $Nu_x/Nu_{fd}=1.00$.

Wu et al. (2001) showed that the entry-length effect is only 1% for Re=100,000. Since at lower Reynolds numbers it should be even smaller, then the effect of thermal-entry-length on refrigerant heat transfer coefficients is negligible in this study since the Reynolds number is <100,000 in the experiments. So, Gnielinski correlation was directly used without any corrections in the model for single phase heat transfer.

A.3.2 Two-phase heat transfer

Wattelet and Chato (1994) correlation was used to calculate refrigerant-side heat transfer coefficient. The correlation equations are given below:

$$h_{ref} = \left[h_{nb}{}^{n} + h_{cb}{}^{n} \right]^{\frac{1}{n}}, \qquad \text{n=2.5} \qquad \text{(A.43)}$$

where h_{nb} = nucleate boiling heat transfer coefficient given by

$$h_{nb} = 55 q''^{0.67} M^{-0.5} P_{r\,0.12} \left[-\log_{10} P_r \right]^{-0.55} \qquad \text{(A.44)}$$

and h_{cb} = convective boiling heat transfer coefficient given by

$$h_{cb} = F h_l R \qquad \text{(A.45)}$$

where

$$F = 1 + 1.925 X_{tt}{}^{-0.83} \qquad \text{(A.46)}$$

$$h_1 = 0.023 \frac{K_l}{d_i} \mathrm{Re}_l\, 0.8\, \mathrm{Pr}_l{}^{0.4} \qquad \text{(A.47)}$$

where k_l = liquid conductivity

$$R = 1.32 Fr_l{}^{0.2}, \qquad \text{for } \mathrm{Fr_l} < 0.25 \qquad \text{(A.48)}$$

$$R = 1, \qquad \text{for } \mathrm{Fr_l} > 0.25 \qquad \text{(A.49)}$$

$$Fr_l = \frac{G_{ref}{}^{2}}{r_l g d_i}, \qquad \text{(A.50)}$$

Appendix B: Comparison of Air-side Heat Transfer and Pressure Drop Correlations

Three plain-fin-round-tube air-side heat transfer and pressure drop correlations: Granryd et al. (1999); Wang et al. (2000); and Kim et al. (1999) collectively spanning a wide range of data were considered.

B.1 Geometry

Table B.1 compares the range of various variables and certain non-dimensional ratios for these correlations with two heat exchangers of open vertical medium temperature display case heat exchanger specifications. Coil H.1 is from a Hussmann M4E case, and coil V.1 is from H Hill-Phoenix OHM case. Figures B.1 to B.3 compares the transverse tube pitch, longitudinal tube pitch, fin pitch, tube outer diameter for the correlations.

Table B.1 Range of variables and non-dimensional parameters for Granryd, Wang and Kim's correlation for plain-fin-round-tube heat exchangers.

Wang et al. (2000)		**Coil H.1**	**Coil V.1**	**Variable**	**Kim et al. (1999)**		**Granryd et al. (1999)**	
Lower bound	Upper bound				Lower bound	Upper bound	Lower bound	Upper bound
6.35	12.7	11.3	12.7	**Dc [mm] Tube collar diameter**	7.3	19.3	0	35
1.19	8.7	8.3	12.7	**Fs [mm] Fin spacing**	0.99	8.55	3	16
12.4	27.5	38.1	25.4	**P_l [mm] Long. tube spacing**	12.7	43.99	33.3	100
17.7	31.75	30.48	48.26	**P_t [mm] Transv. tube spacing**	20.32	50.8	33.3	100
1	6	11	12	**NP [-] No. of tube rows**	1	8	1	3
0.11	0.152	0.168	0.203	**f_{th} [mm] Fin thickness**	0.11	0.406	1.2	1.2
300	10000	~2000	~500	**Re_{Dc} (from graphs)**	505	24707	500	20000
				Ratios				
1.152	1.7	0.8	1.9	**P_t/P_l**	0.857	1.654		
0.092	0.652	0.748	1	**Fs/Dc**	0.081	0.641		
0.039	0.374	0.272	0.263	**Fs/P_t**				
		2.697	3.8	**P_t/Dc**	1.996	2.881		

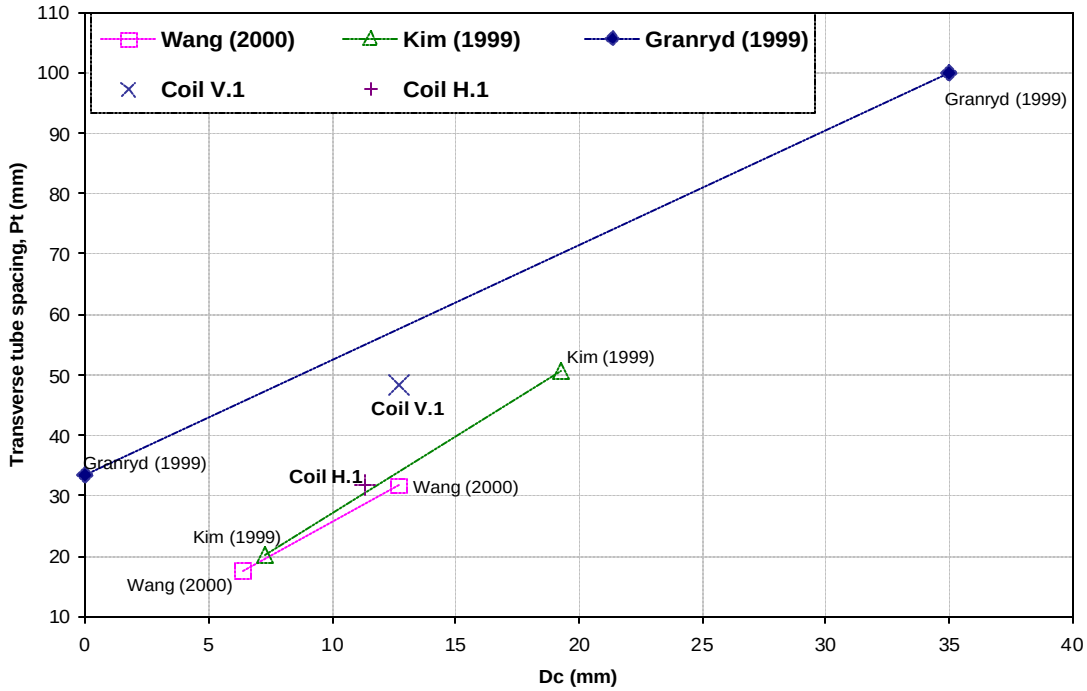

Figure B.1 Transverse tube spacing and tube outer diameter

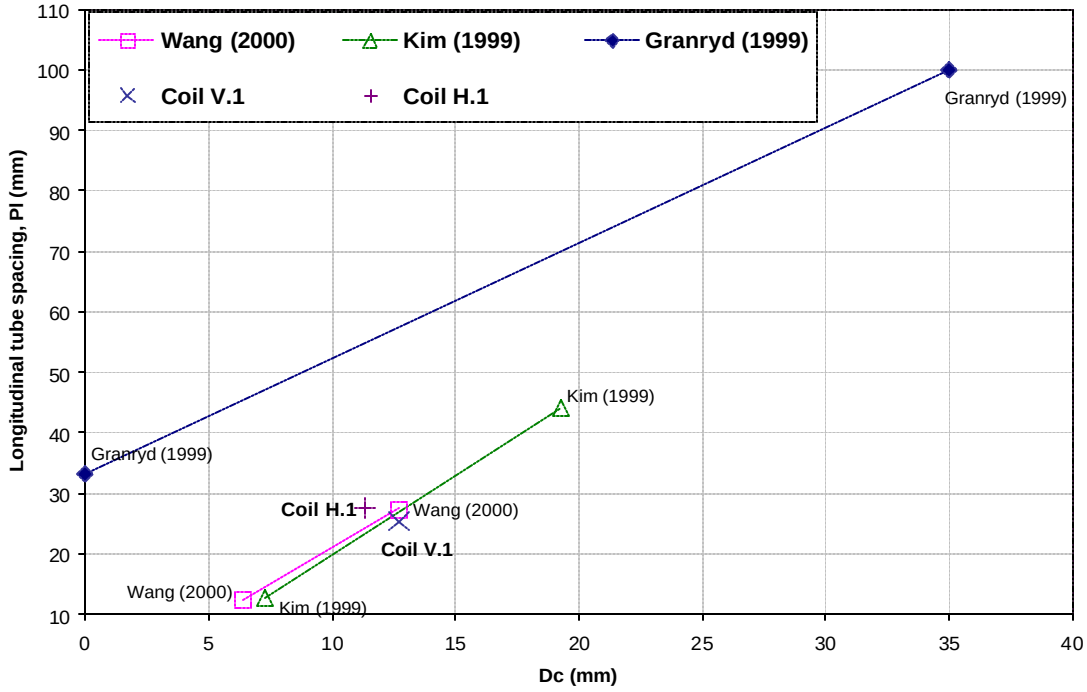

Figure B.2 Longitudinal tube spacing and tube outer diameter

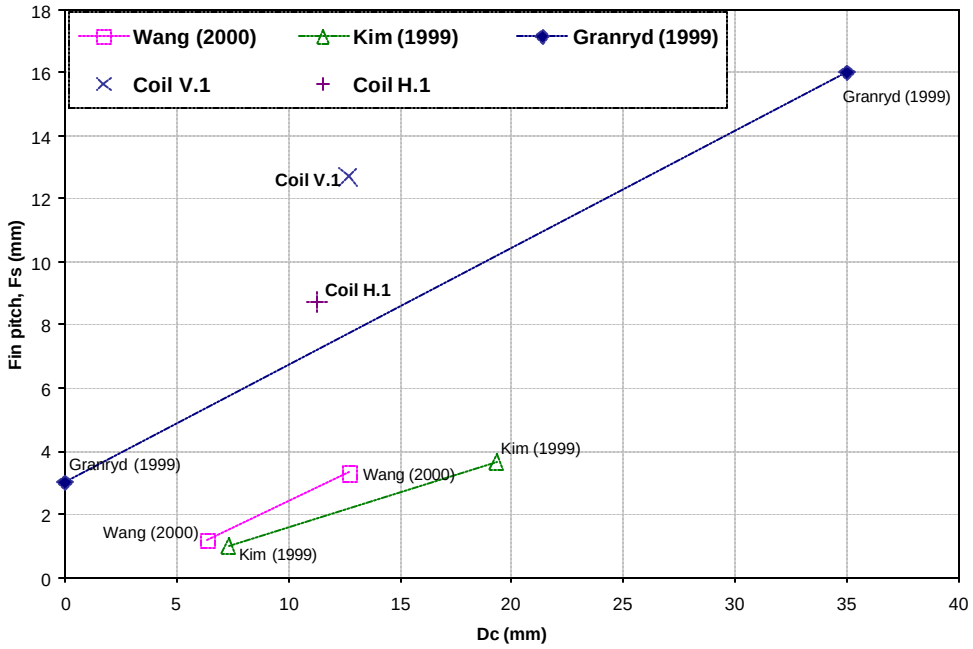

Figure B.3 Fin pitch and tube outer diameter

Dimensionally, both the coils (H.1 and V.1) were well within the range of Kim's and Granryd's correlations and almost on the outer limits of Wang's correlation. However, considering the fact that both Kim's and Wang's correlations had only 3 data points out of 47 and 74 data points respectively, with fin pitches greater than 3.6 mm, it is reasonable to assume that dimensionally both the coils were outside the range of Kim's and Wang's correlations. Non-dimensionally, coil H.1 almost fell on the outer bounds of Wang's correlation while V.1 fell outside the limits of Kim's correlation. Granryd's correlation seems to be the only existing correlation that encompasses both the coils. Fahlen (1996) also used Granryd's air-side heat transfer and pressure drop correlation in his study of frosting and defrosting of air-coils.

B.2 Pressure drop

Figure B.4 compares pressure drop across coils V.1 and H.1 with air flow rates of 300 cfm and 700 cfm respectively under dry conditions as predicted by Kim, Granryd and Wang correlations and tube-plus-fin (dP_finite) superposition.

Kim's correlation was found to highly overestimate the pressure drop (>100%) and was therefore rejected. As expected, the pressure drop predicted using Granryd's correlation was slightly higher than simple tube-plus-fin-superposition, since the Granryd's correlation accounts for the non-linear interaction between fins and tubes coil which is apparently not captured by the simple fin-plus-tube superposition. The pressure drop predicted by Wang's correlation was higher (50% for V.1 and 30% for H.1) than that using Granryd's correlation. Figure B.5 compares the pressure drop predictions for Carlson's experiments with a 8-row coil having a 12.7 mm collar diameter and 8 mm fin spacing (for detailed coil geometry and test conditions see Carlson et al. 2001). Both Granryd and Wang predictions agreed within ± 5% while the tube-plus-fin superposition predicted values as much as 30% below Granryd's values.

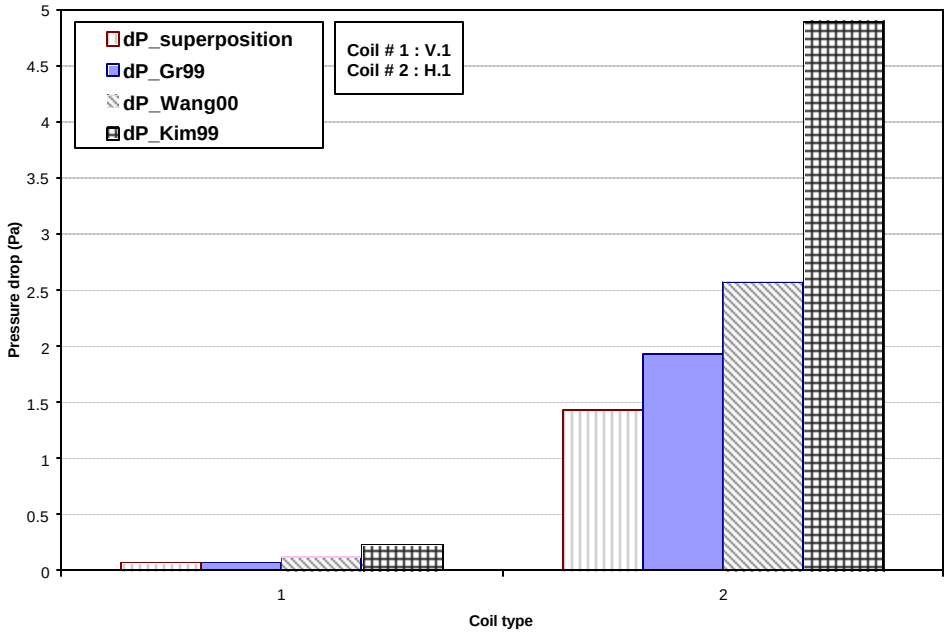

Figure B.4 Pressure drop predictions for coils V.1 and H.1 under dry conditions.

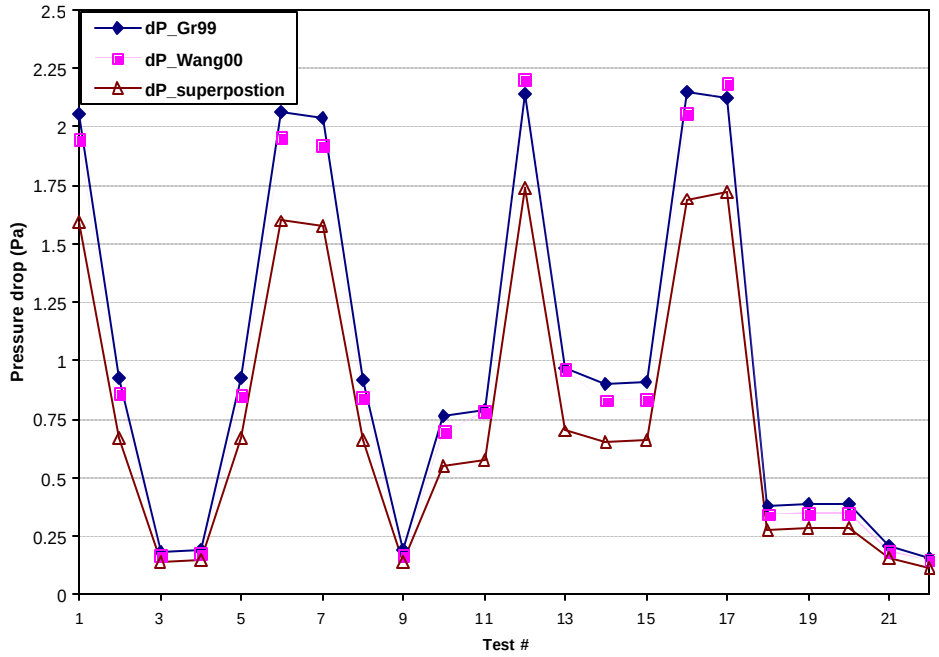

Figure B.5 Pressure drop predictions for dry tests of Carlson et al. (2001).

To further narrow down the selection to one correlation, the effect of varying fin pitch and air flow rate on pressure drop was investigated for both Granryd's and Wang's correlations. Figures B.6 and B.7 depict the effect of varying fin pitch on pressure drop across coils V.1 and H.1 respectively, and Figures B.8 and B.9 depict the effect of varying air flow rate on pressure drop across coils V.1 and H.1 respectively. For both coils, the pressure drop predicted by extrapolating Wang's correlation was found to diverge from the fin-plus-tube superposition for higher

fin pitches where physical considerations suggest that superposition should apply. As expected, extrapolations of Granryd's correlation approached the superposition values (pressure drop across tubes being dominant). Moreover Wang's correlation over-predicted the measured pressure drop across both the coils. With variation of air flow rate however, all three predicted pressure drops varied in a similar manner as seen in Figures B.8 and B.9 with Wang's correlation predicting higher pressure drop at high air flow rates. Therefore Granryd's air-side pressure drop correlation was selected for use in the model.

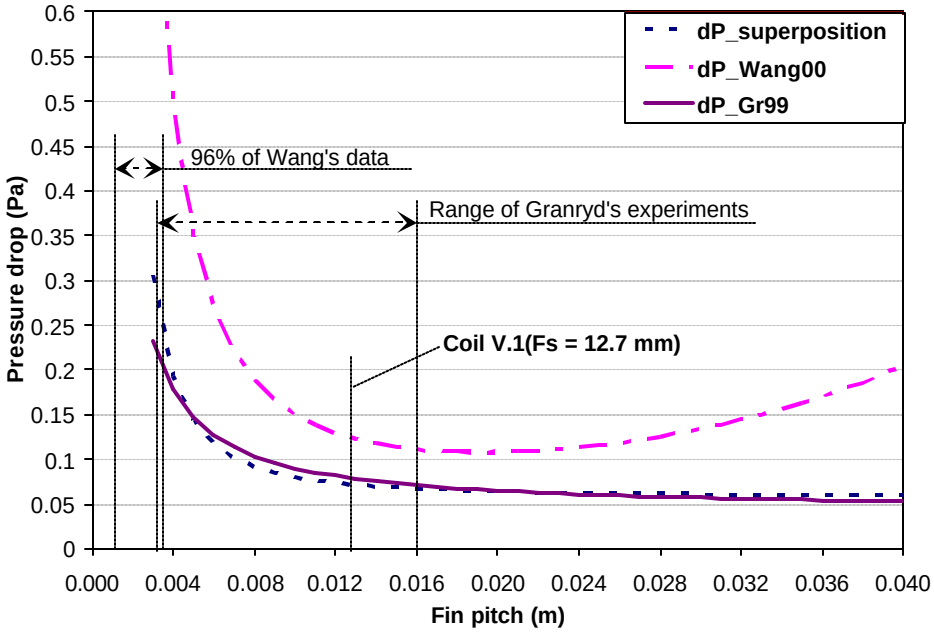

Figure B.6 Effect of fin pitch on pressure drop across coil V.1.

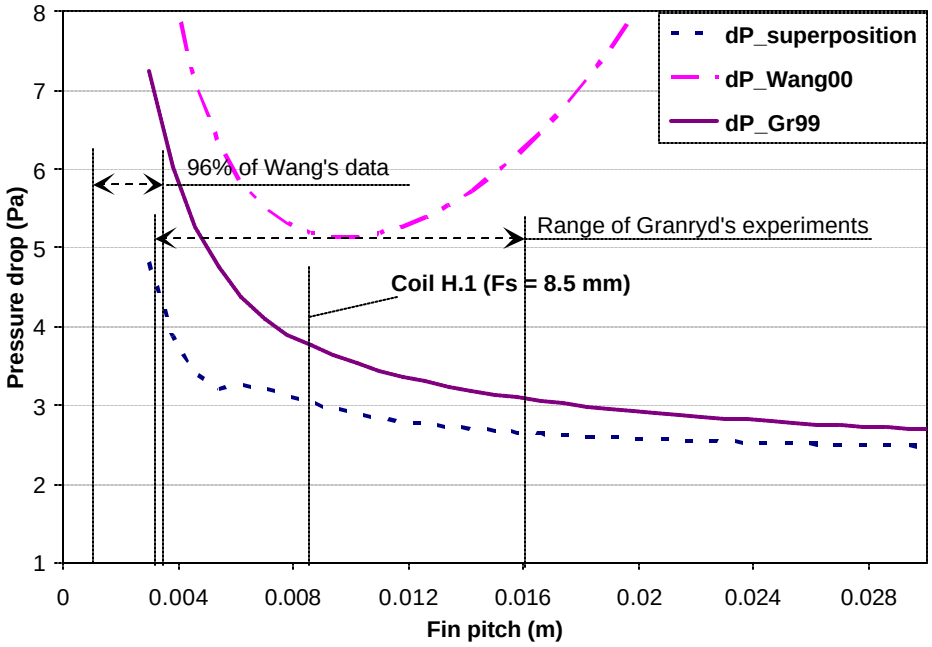

Figure B.7 Effect of fin pitch on pressure drop across coil H.1.

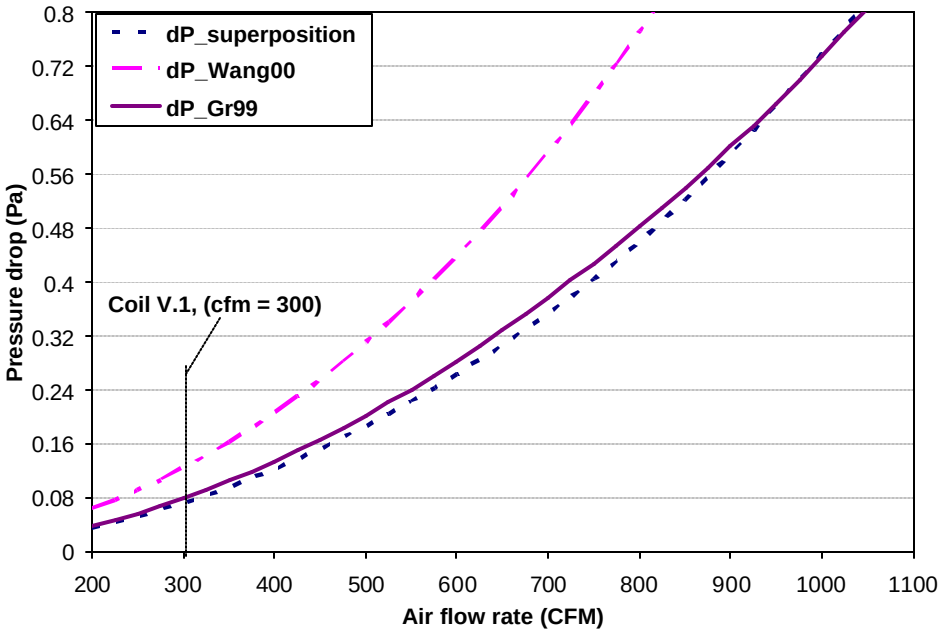

Figure B.8 Effect of air flow rate on pressure drop across coil V.1.

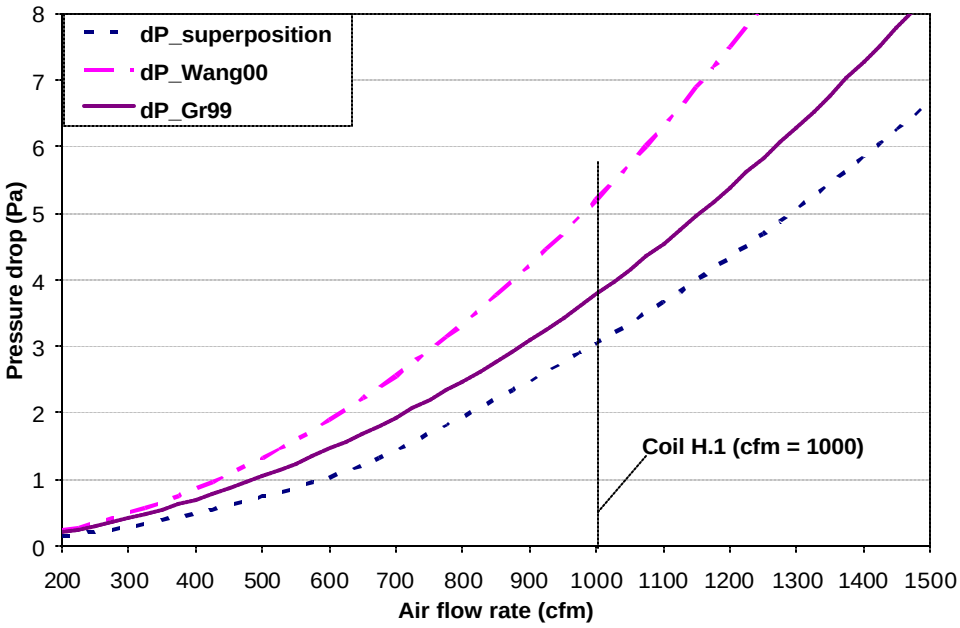

Figure B.9 Effect of air flow rate on pressure drop across coil H.1.

B.3 Heat transfer

Figure B.10 compares the heat transfer coefficient predictions for Carlson's experiments with an 8-row coil having a 12.7 mm collar diameter and 8 mm fin spacing (for detailed coil geometry and test conditions see Carlson et al. 2001). Both Granryd and Wang predictions agreed within ± 7% and within 10% of Carlson's predictions, while Kim's correlation predicted values as much as 22% more than Carlson's experimental predictions.

Figure B.11 compares air-side heat transfer for coils V.1 and H.1 with air flow rates of 300 cfm and 700 cfm respectively under dry conditions as predicted by Kim, Granryd and Wang and Carlson correlations. Kim's

correlation was found to highly overestimate the heat transfer coefficient (> 50%) and was therefore rejected. Since Carlson's correlation was mere a simple scaling (78 %) of Kim's correlation, it also over-predicted the heat transfer coefficient in comparison to Wang's and Granryd's correlations which agreed with one another. Hence Kim's and Carlson's correlation were dropped from consideration.

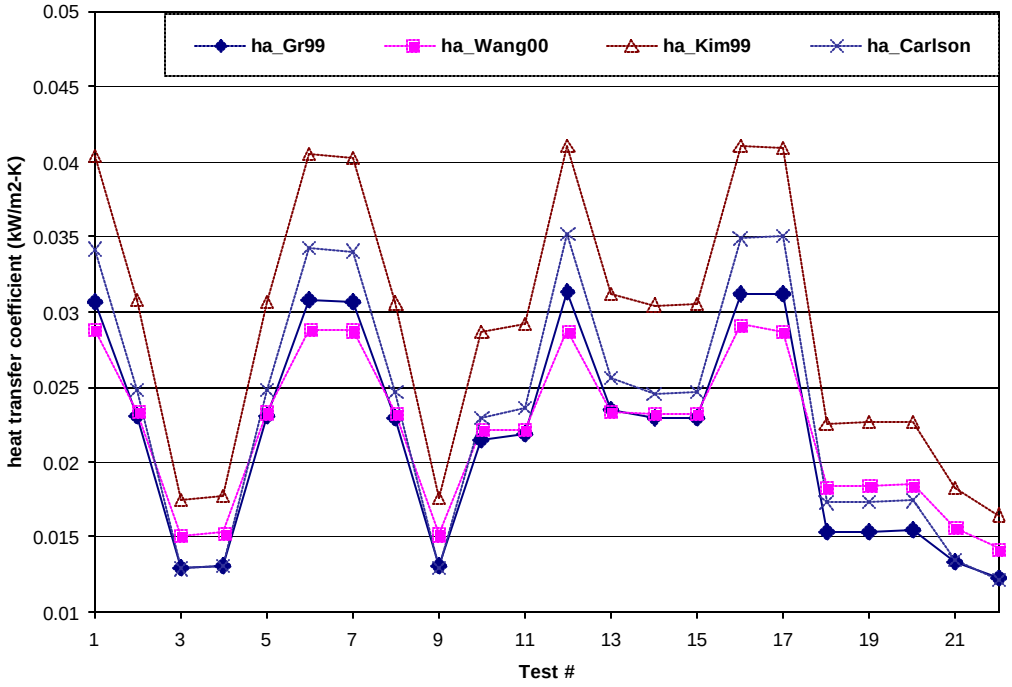

Figure B.10 Heat transfer coefficient for dry tests of Carlson et al. (2001).

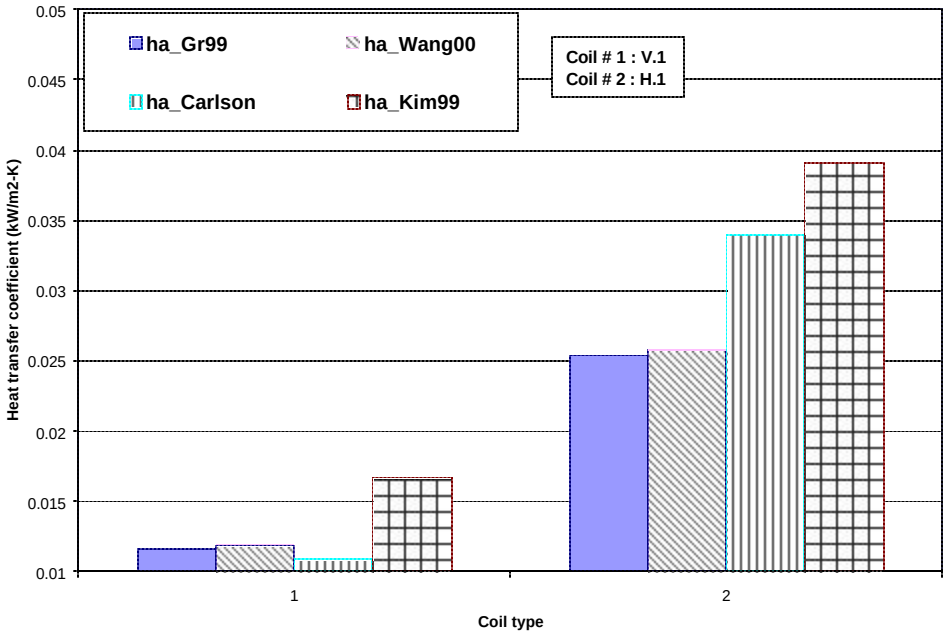

Figure B.11 Heat transfer coefficient for coils V.1 and H.1 under dry conditions.

To further narrow down the selection to one correlation, the effect of varying fin pitch and air flow rate on pressure drop was investigated for both Granryd's and Wang's correlations. Figures B.12 and B.13 depict the effect of varying fin pitch on heat transfer coefficient predictions for coils V.1 and H.1 respectively, and Figures B.14 and B.15 depict the effect of varying air flo w rate on heat transfer coefficient for coils V.1 and H.1 respectively. Clearly the Kim's correlation over-predicted the heat transfer correlation for both the coils and due to the nature of correlation it was insensitive to the effect of varying fin pitch. While the Wang's and Granryd's correlation predicted almost same heat transfer coefficient values and its variation with air flow rate as shown in Figures B.14 and B.15, the pitfalls of Wang's correlation become obvious when looking at variations of heat transfer coefficient with fin pitch. With increasing fin pitch the heat transfer coefficient should increase approaching the value for tube banks only. Granryd's predictions are of the same nature while Wang's correlation predicted an opposite trend. Therefore Granryd's air-side heat transfer correlation was selected for use in the model.

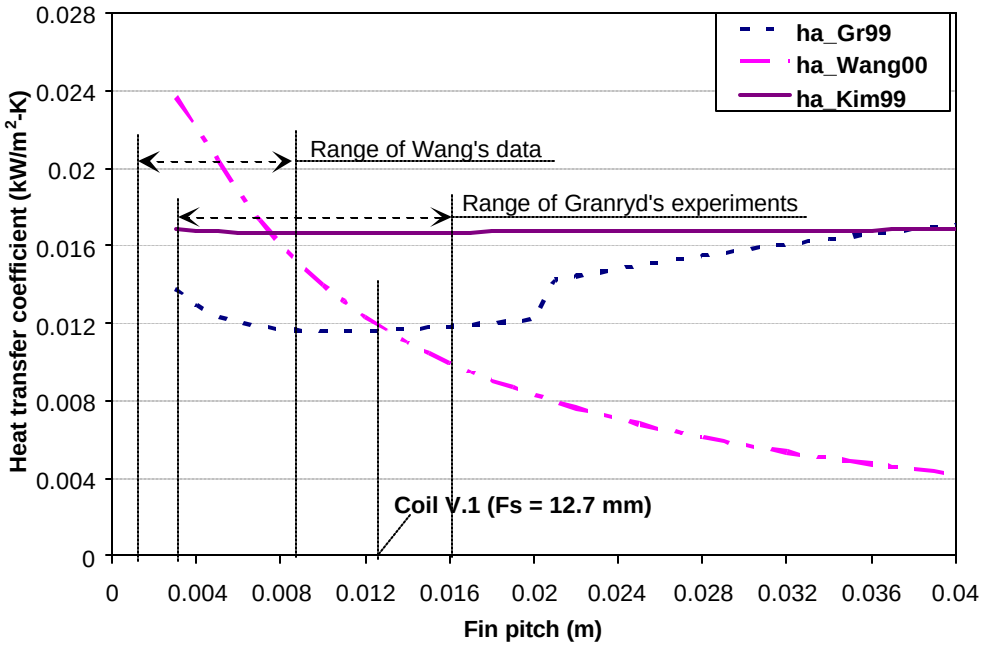

Figure B.12 Effect of fin pitch on heat transfer coefficient for coil V.1.

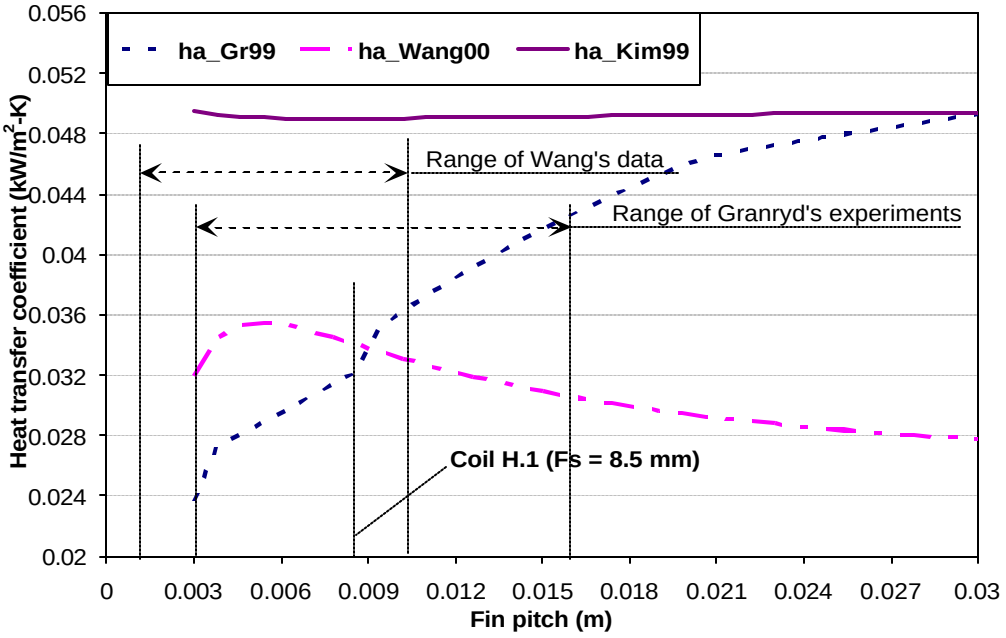

Figure B.13 Effect of fin pitch on heat transfer coefficient for coil H.1.

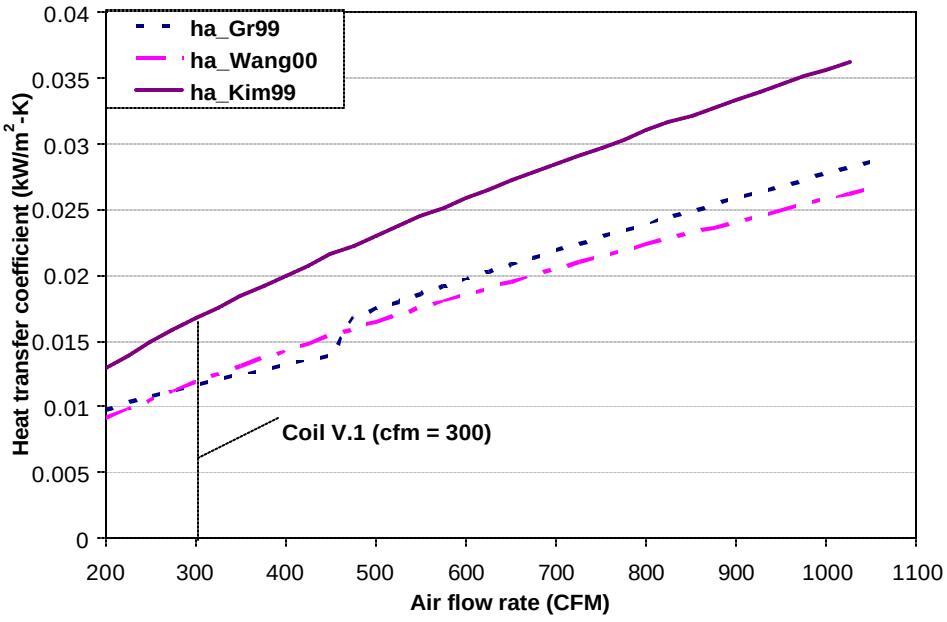

Figure B.14 Effect of air flow rate on heat transfer coefficient for coil V.1.

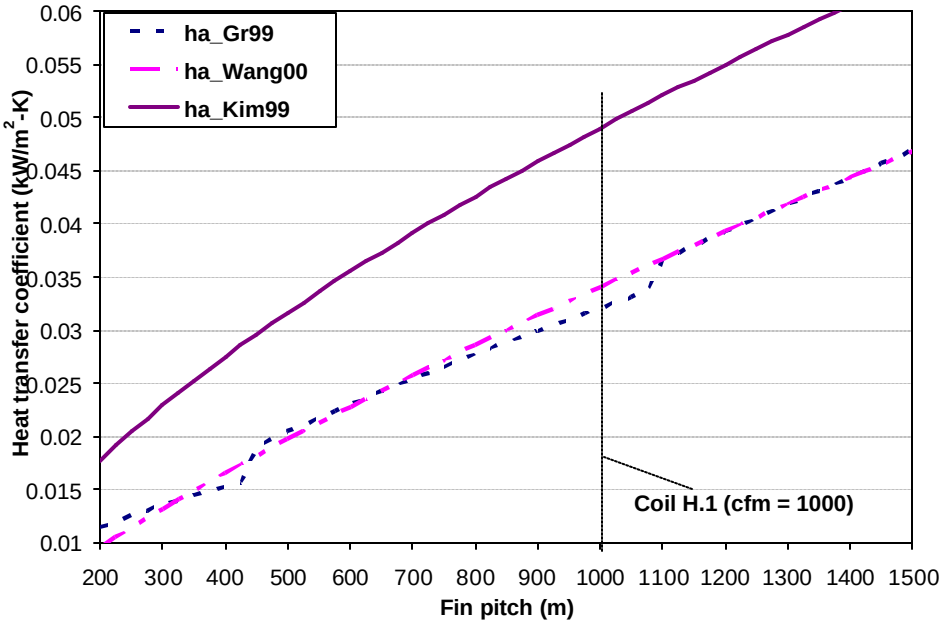

Figure B.15 Effect of air flow rate on heat transfer coefficient for coil H.1.

Appendix C: Frost and fin Conduction

C.1 One-two-and-three-lump modeling of frost and fin conduction

Previous researchers have modeled the frost formation on fin as a wet fin surface efficiency neglecting the conduction along the frost and implicitly handling the frost surface temperature. For our simulation model, the frost surface temperature was an explicit parameter as it determined the frost density, hence its conductivity. Thus a different but physically viable analysis was done to model frost growth on fin surface. After calculating convective heat and mass transfer to the frost layer, conduction to the tube was modeled long two paths: (i) from frost directly to fin base; and (ii) from frost to the fin and then along the fin to the fin base.

Analysis was done assuming one, two, three lumps models of homogenous frost and fin masses along the fin length. Comparisons were done for all the models and the results are presented below. Figures C.1 and C.2 show one-and two-lump models, respectively. The total heat transfer, Q_{total} is determined as a sum of sensible and latent heat transfer. The sensible heat transfer is determined from the air temperature gradient at the frost surface (and air-side heat transfer coefficient) while the latent heat (and mass) transfer is determined from the corresponding humidity gradient. Since the objective of this analysis was to determine the resolution of lumped models needed to determine the representative frost surface and fin temperatures, the total heat transfer was assumed to be 60% more than the sensible heat transfer to avoid mass transfer complications for this simple analysis. This assumption was consistent with the display case data for the first time step during frosting cycle.

For a single lump model as shown in Figure C.1, the average temperature T_1 of frost lump was defined as the average of the frost outer and inner surface temperatures: T_{so} and T_f, respectively. Both the frost and the fin lumps were assumed to contact the tube collar at the same base temperature T_{si}. As seen in Figure 1, the total heat transfer from the air to the frost was divided into two parts: Q_{2si} from fin (T_f) to base (T_{si}); and conduction Q_{1si} from frost (T_1) to base (T_{si}) parallel to the fin. The conduction heat transfer from frost to fin (transverse to frost thickness), Q_{12} is equal to the conduction down the fin, Q_{2si}.

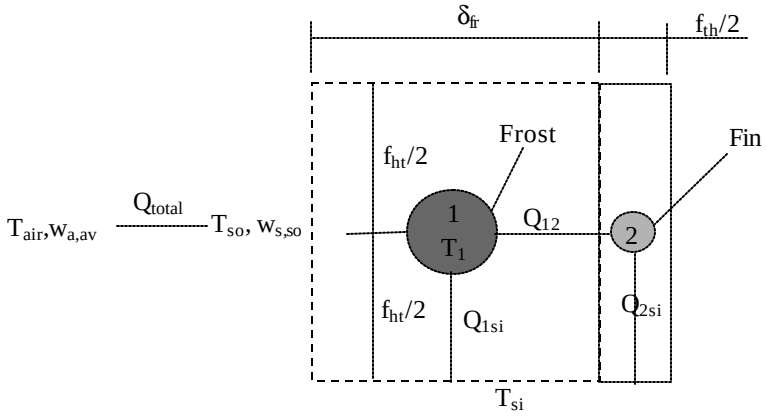

Figure C.1 Single lump model

$$Q_{1si} = \left(\frac{k_{fr}}{f_{ht}/2} \right) d_{fr} .(T_1 - T_{si}) \qquad \text{(C.1)}$$

$$Q_{2si} = \left(\frac{k_{fin}}{f_{ht}/2} \right) \frac{f_{th,0}}{2} .(T_2 - T_{si}) \quad \text{(C.2)}$$

$$Q_{12} = \left(\frac{k_{fr}}{d_{fr}/2} \right) f_{ht} .(T_1 - T_2) = Q_{2si} \quad \text{(C.3)}$$

$$Qt = 1.6.Q_{sens} = 1.6.h_{air} .f_{ht} .(T_{air} - T_{so}) \quad \text{(C.4)}$$

$$Q_t = Q_{1si} + Q_{2si} \quad \text{(C.5)}$$

For the two-lump model, frost and fin were divided into two lumps each as shown in Figure C.2. Each frost lump was modeled for a different frost surface ($T_{so,1}$ and $T_{so,3}$) and average temperatures (T_1 and T_3). The total heat transfer was divided into two parts ($Q_{t,1}$ and $Q_{t,2}$), one each for each frost lump and each was assumed to be 60% greater than the respective sensible heat transfer. The top frost lump conducted heat to bottom frost lump (Q_{13}) and corresponding fin lump (Q_{12}) while the bottom frost lump conducted heat to the corresponding fin lump (Q_{34}) and to the base (Q_{3si}). The top fin lump would conduct heat to the bottom fin lump (Q_{24}) while the bottom fin lump conducted heat to the base (Q_{4si}).

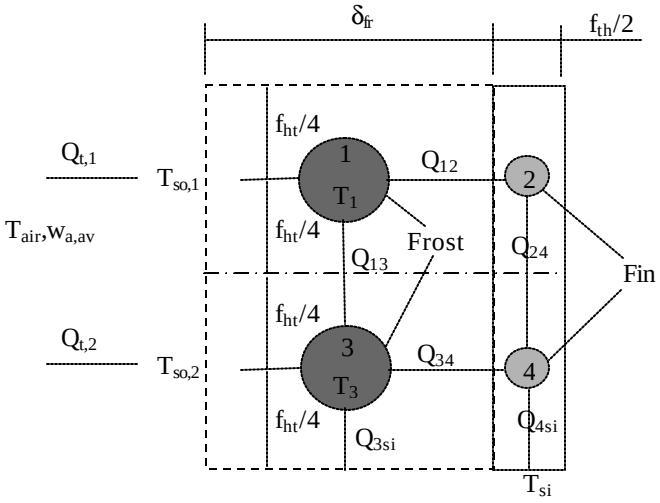

Figure C.2 Two lump model

$$Q_{12} = \left(\frac{k_{fr}}{d_{fr}/2} \right) \frac{f_{ht}}{2} .(T_1 - T_2) \quad \text{(C.6)}$$

$$Q_{34} = \left(\frac{k_{fr}}{d_{fr}/2} \right) \frac{f_{ht}}{2} .(T_3 - T_4) \quad \text{(C.7)}$$

$$Q_{13} = \left(\frac{k_{fr}}{f_{ht}/2} \right) d_{fr} .(T_1 - T_3) \quad \text{(C.8)}$$

$$Q_{24} = \left(\frac{k_{fin}}{f_{ht}/2} \right) \frac{f_{th,0}}{2} .(T_2 - T_4) = Q_{12} \quad \text{(C.9)}$$

$$Q_{3si} = \left(\frac{k_{fr}}{f_{ht}/4} \right) d_{fr} .(T_3 - T_{si}) \quad \text{(C.10)}$$

$$Q_{4si} = \left(\frac{k_{fin}}{f_{ht}/4} \right) \frac{f_{th,0}}{2} .(T_4 - T_{si}) \quad \text{(C.11)}$$

$$Q_{t,1} = 1.6.Q_{sens,1} = 1.6.h_{air} . \frac{f_{ht}}{2} .(T_{air} - T_{so,1}) \quad \text{(C.12)}$$

$$Q_{t,2} = 1.6.Q_{sens,2} = 1.6.h_{air} . \frac{f_{ht}}{2} .(T_{air} - T_{so,2}) \quad \text{(C.13)}$$

$$Q_{13} + Q_{t,,2} = Q_{34} + Q_{3si} \quad \text{(C.14)}$$

$$Q_{24} + Q_{34} = Q_{4si} \quad \text{(C.15)}$$

$$Q_t = Q_{t,1} + Q_{t,2} = Q_{3si} + Q_{4si} \quad \text{(C.16)}$$

For three-lump model, frost and fin was divided into three lumps each and the analysis was done in a manner similar to that of two-lump model.

C.2 Results

Figure C.3 and C.4 compare the average fin and frost surface temperatures, respectively for single, two and three lumps models for variations in the frost thickness. As seen in Figures, the frost surface temperature and fin temperature for single lump model is ~0.3 ^{o}C higher than the average frost surface temperature and average fin temperature respectively of two and three lump models. This is due to ~8% lower heat transfer per unit width for single lump model as compared to two and three lumps models as shown in Figure C.5.

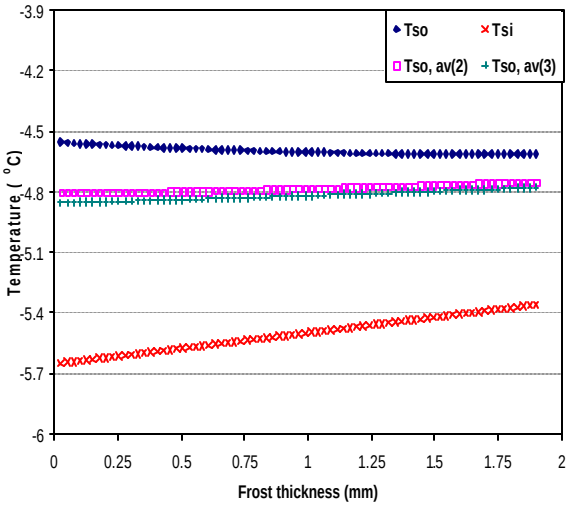

Figure C.3 Frost surface and base temperatures

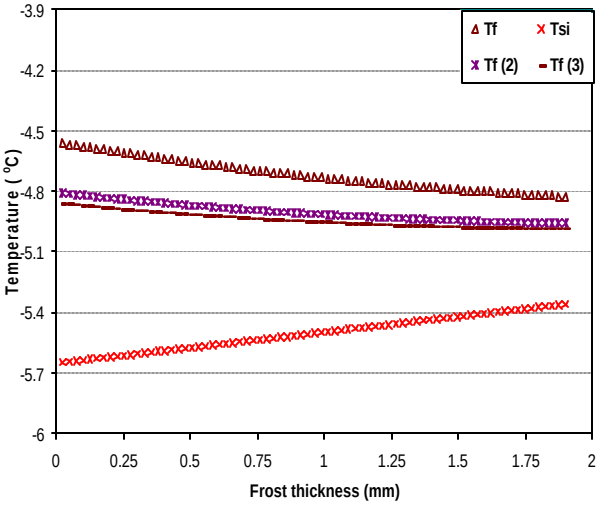

Figure C.4 Fin and base temperatures

The two-and three-lump models agreed within 1% of each other, so the two-lump model was found accurate enough in predicting the average frost surface and average fin temperatures. Hence the two-lump model was implemented in the model simulations.

Figure C.6 compares the conduction heat transfer from frost and fin to base with variation in frost thickness. The heat transfer from frost to base is negligible when the frost layer is thin. However it contributes to as much as 26% with 1.9 mm of frost being deposited on the surface of the fin. Thus the conduction heat transfer through frost directly to the tube collar can no longer be neglected in comparison to the conduction through the fin.

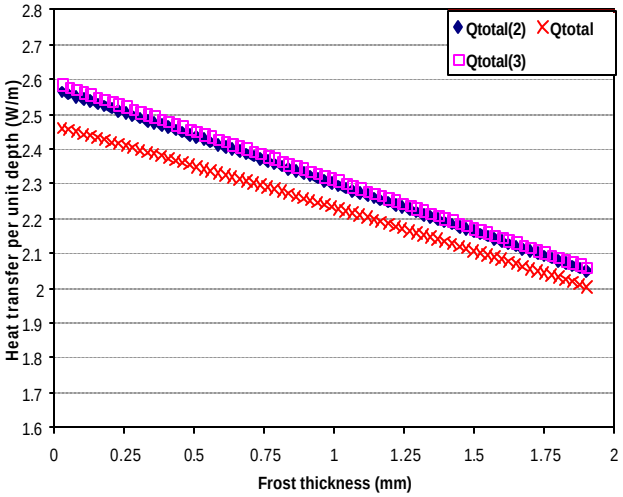

Figure C.5 Heat transfer per unit width

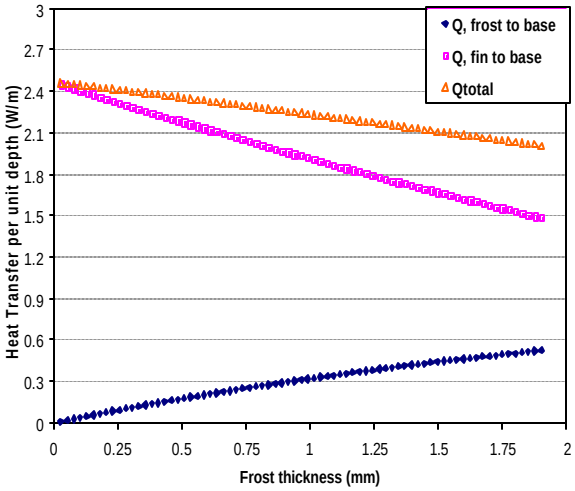

Figure C.6 Fin and frost conduction

Bibliography

Ameen, F. R. 1993. Study of Frosting on Heat Pump Evaporators. *ASHRAE Transactions* 99:61-71.

Carlson, D. M., P. S. Hrnjak, and C. W. Bullard. 2001. Deposition, distribution, and effects of frost on a multi-row heat exchanger performance. *Air Conditioning and Refrigeration Center, University of Illinois at Urbana-Champaign, IL* TR-183.

Chen, H., L. Thomas, and R.W. Besant. 2000. Modeling Frost Characteristics on Heat Exchanger Fins: Pt. I, Numerical Model. *ASHRAE Transactions* 106, Pt.2.

Chen, H., L. Thomas, and R. W. Besant. 2000. Modeling Frost Characteristics on Heat Exchanger Fins: Pt. II, Model Validation and Limitations. *ASHRAE Transactions* 106, Pt.2.

Churchill, S. W. 1977. Friction-factor equation spans all fluid-flow regimes. *Chemical Engineering* pp 91-92.

Davis M. A., A. M. Jacobi, and P. S. Hrnjak. 1996. Evaporator calorimeter: The study of overall heat transfer performance. *Air Conditioning and Refrigeration Center, University of Illinois at Urbana-Champaign, IL* TR-107.

Gnielinski, V. 1976. New equations for heat and mass transfer in turbulent pipe and channel flow. *Chemical Engineering*, 16:359-368.

Granryd E., E. Ingvar, P. Lundqvist, A. Melinder, B. Palm, and P. Rohlin. 1999. Refrigeration and Engineering, *Department of Engineering Technology, Division of Applied Thermodynamics and Refrigeration, Royal Institute of Technology, KTH, Stockholm.*

Hayashi, Y., K. Aoki, and H. Yuhura. 1976. Study of frost formation based on a theoretical model of the frost layer. *Trans. Japan Society Mechanical Engineers* 40:885-899.

Hayashi, Y., A. Aoki, S. Adachi, and K. Hori. 1977. Study of frost properties correlation with frost formation types. *Journal of Heat transfer* 99: 239-245.

Hoke, J. L., J. G. Georgiadis, and A. M. Jacobi. 2000. The Interaction between the Substrate and Frost Layer through Condensate distribution. Ph.D. Dissertation. *University of Illinois at Urbana-Champaign.*

Itoh, M., H. Kogure, S. Yoshinaga, R. Hoshino, N. Wakabayashi, M. Kudoh, and H. Kusumoto. 1996. Experimental Study on Parallel-Flow-Type Heat Exchangers for Residential Heat Pump Systems. *Proceedings of the 1996 JAR Annual Conference* pp 73-76.

Jones, B. W., and J. D. Parker. 1975. Frost formation with varying environmental parameters. *Trans. Journal of Heat Transfer* 97(2):255-259.

Kim, N. H., B. Youn, and R. L. Webb. 1999. Air-Side Heat Transfer and Friction Correlations for Plain Fin-and-Tube Heat Exchangers with Staggered Tube Arrangements. *Transactions of ASME* 121:662-667.

Kondepudi, S. N., and D. L. O'Neal. 1987. The effect of frost growth on extended surface heat exchanger performance—a review. *ASHRAE Transactions* 93(2):258-274.

Kondepudi, S. N., and D. L. O'Neal. 1989. Performance of Finned Tube Heat Exchangers under Frosting Conditions. *ASME – HTD* 123:193-200.

Kondepudi, S.N., and D. L. O'Neal. 1990. The effects of different fin configurations on the performance of finned-tube heat exchangers under frosting conditions. *ASHRAE Transactions* 96(2).

Kondepudi, S. N., and D. L. O'Neal. 1991. Frosting Performance of Tube Fin Heat Exchangers with Wavy and Corrugated Fins. *Experimental Thermal and Fluid Science* 4:613-618.

Marinyuk, B. T. 1980. Heat and Mass Transfer under Frosting Conditions. *International Journal of Refrigeration* 3(6):366-368.

Mao Y., R. W. Besant, and H. Chen. 1999. Frost Characteristics and Heat Transfer on a Flat Plate under Freezer Operating Conditions: Pt. I, Experimentation and Correlations. *ASHRAE Transactions* 105(2):231-251.

Ogawa, K., N. Tanaka, and M. Takeshita. 1993. Performance Improvement of Plate Fin-and-tube Heat Exchangers under Frosting Conditions. *ASHRAE Transactions* 99: 762-771.

O'Neal, D. L., and D. R. Tree. 1985. A review of frost formation in simple geometries. *ASHRAE Transactions* 91:267-281.

Oskarsson, S. O., K. I. Krakow, and S. Lin. 1990. Evaporator models for operation with dry, wet and frosted finned surfaces, Pt. I and II. *ASHRAE Transactions* 96(1): 373-392.

Ostin, R., and S. Andersson. 1991. Frost Growth Parameters in a Forced Air Stream. *Int. J. Heat Mass Transfer* 34(4-5):1009-1017.

Padki, M. M., S. A. Sherif, and R. M. Nelson. 1989. A simple method for modeling the frost formation phenomenon in different geometries. *ASHRAE Transactions* 95(2): 1127-1137.

Raju, S. P. and S. A. Sherif. 1993. Frost Formation and Heat Transfer on Circular Cylinders in Cross-Flow. *International Journal of Refrigeration* 16(3):390-402.

Rite, R. W., and R. R. Crawford. 1990. The effect of frosting on the performance of domestic refrigerator-freezer finned tube evaporator coils. *Air Conditioning and Refrigeration Center, University of Illinois at Urbana-Champaign, IL* TR-01.

Sanders C. Th. 1974. Frost formation: The influence of frost formation and defrosting on the performance of air coolers. Ph.D. Thesis. *Technique Hogeschool, Delft, Netherlands.*

Senshu, T., H. Yasuday, K. Oguni, and K. Ishibane. 1990. Heat pump performance under frosting conditions Part 1 and 2. *ASHRAE Transactions* 96(1):324-336.

Souza A. L., and M. M. Pimenta. 1995. Prediction of pressure drop during horizontal two-phase flow of pure and mixed refrigerants. *ASME Conf. Cavitation and multiphase flow, HTD* 210:161-171.

Storey, B.D., and A. M. Jacobi. 1999. The Effect of Streamwise Vortices on the Frost Growth Rate in Developing Laminar Channel Flows. *International Journal of Heat and Mass Transfer* 42:3787-3802.

Tassau, S. A., and D. Datta. 1999. Influence of Supermarket Environmental Parameters on the Frosting and Defrosting of Vertical Multideck Display Cabinets. *ASHRAE Transactions* 105(1):491-496.

Tao, Y.X., R. W. Besant, and K. S. Rezkallah. 1993. A Mathematical Model for Predicting the Densification and Growth of Frost on a Flat Plate. *Int. J. Heat Mass Transfer* 36(2):353-363.

Threlkeld, J.L. 1970. *Thermal Environmental Engineering (2nd Edition)*, Prentice-Hall, New York, N.Y.

Verma P., D. M. Carlson, Y. Wu, C. W. Bullard, and P. S. Hrnjak. 2002. Experimentally validated model for frosting of plain-fin-round-tube heat exchanger. *IIR conference, "New Technologies in Commercial Refrigeration".*

Wang, C. C., Y. J. Chang, Y. C. Hsieh, and Y. T. Lin. 1996. Sensible Heat and Friction Characteristics of Plate Fin-and-Tube Heat Exchangers Having Plane Fins. *Int. J. of Refrigeration* 19(4):223-230.

Wang, C. C., and C. T. Chang. 1998. Heat and Mass Transfer for Plate Fin-and-Tube Heat Exchangers, With and Without Hydrophilic Coating. *Int. J. Heat and Mass Transfer* 41:3109-3120.

Wang, C. C., K. Y. Chi, and C. J. Chang. 2000. Heat transfer and friction characteristics of plain fin-and-tube heat exchangers, Part II: Correlation. *Int. J. of Heat and Mass Transfer* 43(15): 2693-2700.

Wattelet, J. P., and J. C. Chato. 1994. Heat transfer flow regimes of refrigerants in a horizontal-tube evaporator. *Air Conditioning and Refrigeration Center, University of Illinois at Urbana-Champaign, IL* TR-55.

Watters, R. J., D. L. O'Neal, and J. Yang. 2002. Frost/defrost performance of a three-row fin staged heat pump evaporator. *ASHRAE Transactions* 108(2).

Wu, Y., Verma, P., Bullard, C. W., and Hrnjak, P. S. 2001. Simulating the performance of a heat exchanger during frosting. *Air Conditioning and Refrigeration Center, University of Illinois at Urbana-Champaign, IL* TR-186.

Yonko, J. D., and. C. F. Sepsy. 1967. An investigation of the thermal conductivity of frost while forming on a flat horizontal plate. *ASHRAE Transactions* 73(II): I.1.1-I.1.11.